Theory of spiral wave dynamics in weakly excitable media: Asymptotic reduction to a kinematic model and applications

Vincent Hakim[1] and Alain Karma[2]
[1]*Laboratoire de Physique Statistique,* Ecole Normale Supérieure, 24 rue Lhomond, 75231 Paris Cedex 05, France*
[2]*Department of Physics and Center for Interdisciplinary Research on Complex Systems, Northeastern University, Boston, Massachusetts 02115*
(Received 18 March 1999)

In a weakly excitable medium, characterized by a large threshold stimulus, the free end of an isolated broken plane wave (wave tip) can either rotate (steadily or unsteadily) around a large excitable core, thereby producing a spiral pattern, or retract, causing the wave to vanish at boundaries. An asymptotic analysis of spiral motion and retraction is carried out in this weakly excitable large core regime starting from the free-boundary limit of the reaction-diffusion models, valid when the excited region is delimited by a thin interface. The wave description is shown to naturally split between the tip region and a far region that are smoothly matched on an intermediate scale. This separation allows us to rigorously derive an equation of motion for the wave tip, with the large scale motion of the spiral wave front slaved to the tip. This kinematic description provides both a physical picture and exact predictions for a wide range of wave behavior, including (i) steady rotation (frequency and core radius), (ii) exact treatment of the meandering instability in the free-boundary limit with the prediction that the frequency of unstable motion is half the primary steady frequency, (iii) drift under external actions (external field with application to axisymmetric scroll ring motion in three dimensions, and spatial- or/and time-dependent variation of excitability), and (iv) the dynamics of multiarmed spiral waves with the prediction that steadily rotating waves with two or more arms are linearly unstable. Numerical simulations of FitzHugh-Nagumo kinetics are used to test several aspects of our results. In addition, we discuss the semi-quantitative extension of this theory to finite cores and pinpoint mathematical subtleties related to the thin interface limit of singly diffusive reaction-diffusion models. [S1063-651X(99)01610-4]

PACS number(s): 82.40.Bj, 47.20.Hw, 87.18.−h

I. INTRODUCTION

Spiral waves are characteristic structures of excitable media [1,2] that have been observed in systems as different as catalytic surface oxidation [3], the Belousov-Zhabotinsky chemical reaction [4–7], aggregating colonies of slime mold [8], and heart tissue where they are suspected to play an essential role in cardiac arrhythmia and fibrillation [9]. Spiral waves are prone to a variety of instabilities, the best studied of which is meander, and they can be made to drift and be controlled in diverse ways, for instance, by varying the medium excitability in space or/and time, or by adding an external field.

Much of the observed experimental phenomenology has been reproduced by using simplified two-variable activator-controller types of description, like the classic FitzHugh-Nagumo (FN) model [10] and mild variations of it. Extensive surveys [11,12] of the possible types of wave motion in such models have been performed in a reduced parameter space where the only two parameters left to vary are the medium excitability Δ, defined in Sec. II in such a way that the isolated pulse speed is proportional to Δ for weak excitability, and the ratio ϵ between the time scale of the activator and controller kinetics, which controls the abruptness of the wave front (i.e., the thickness of the interface delimiting the excited region). Different regimes have been identified that are summarized in Fig. 1 for simple FN kinetics [13]. In the whole region above the *propagation* boundary (∂P), the medium excitability is too weak for any plane wave to propagate persistently. In the narrower region comprised between

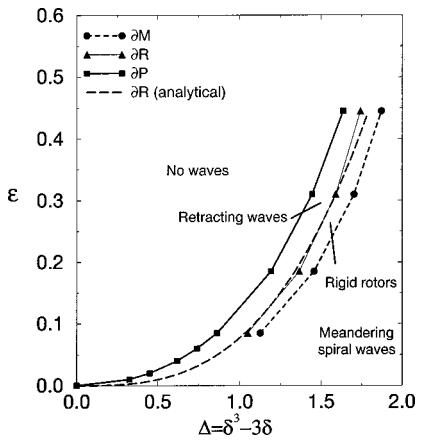

FIG. 1. Plots of the propagation (∂P), rotor (∂R), and meander (∂M) boundaries in the parameter space ϵ (the ratio of the fast activator to the slower controller time scale) and Δ (the medium ''excitability'' defined as $v_s - v_0$) for the numerically simulated FitzHugh-Nagumo kinetics $[f(u,v) = 3u - u^3 - v, g(u,v) = u - \delta]$. Our analysis predicts that the three boundaries smoothly approach the origin without crossing as $\epsilon \to 0$, with $\Delta_p \sim -\epsilon^{1/2} \ln \epsilon$ for ∂P, $\Delta_c \sim \epsilon^{1/3}$ for ∂R, and $\Delta_m - \Delta_c \sim -\epsilon^{5/9}/(\ln \epsilon)^{2/3}$ for ∂M. The prediction $\Delta_c = (2^{1/2} 4\epsilon/B_c)^{1/3}$ with $B_c = 0.535$ for the ∂R boundary is in good agreement with the simulations.

*Associé au CNRS et aux Universités Paris VI et VII.

 © 1999 The American Physical Society

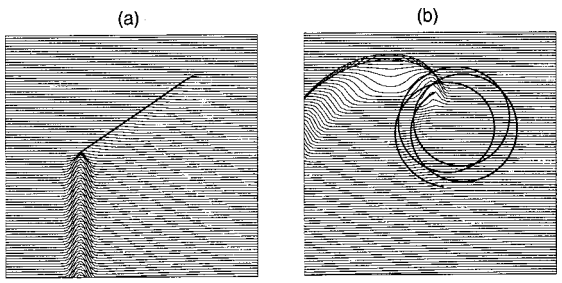

FIG. 2. Surface plots of u and wave tip trajectories (thick solid line) illustrating in (a) a retracting wave for $\delta=-1.4$ and $\epsilon=0.27$, in between the ∂P and ∂R boundaries, and in (b) a large core meandering spiral wave for $\delta=-1.4$ and $\epsilon=0.18$, close to the ∂M boundary.

∂P and the *rotor* boundary (∂R), the medium excitability is sufficient for a plane wave to propagate but not for a spiral wave to form. In this region, the end of a broken wave front, referred to hereafter as the ''wave tip,'' simply retracts steadily [Fig. 2(a)], such that this finger-shaped wave must shrink in length and eventually vanish at boundaries in a finite system. In the even narrower region comprised between ∂R and the *meander* boundary (∂M), the excitability is sufficient for large core spirals to form and the wave tip now rotates steadily at a frequency ω_1 around a circular core of radius R_0. Right on the ∂R boundary, a half plane wave, referred to hereafter as the ''critical finger,'' propagates without changing its shape. It can be equivalently interpreted as a retracting finger with vanishing retracting velocity or as a spiral wave of infinite core radius. As one keeps increasing the excitability, the radius of the spiral core decreases and below the ∂M boundary the spiral tip traces a classic ''flowerlike'' meander pattern [Fig. 2(b)]. It has been shown that meander originates from a supercritical Hopf bifurcation at ∂M which adds a second frequency ω_2 to the basic spiral rotation [14,15]. The meander patterns exhibit first inward petals as $\omega_2<\omega_1$. Outward petals appear as ω_2 becomes greater than ω_1. Further away from ∂M, the spiral tip motion becomes more complex and possibly chaotic past the still poorly characterized ∂C boundary [12] (not shown in Fig. 1). Given that a Hopf bifurcation takes place on ∂M, symmetry arguments fix its resonant coupling to the translation modes when $\omega_2=\omega_1$ and thus determine the bifurcation structure of the tip motion near the codimension 2 point $\omega_2=\omega_1$ on ∂M [16,17].

In contrast to this rather detailed knowledge, the precise mechanisms that govern spiral formation and motion remain less well understood from both physical and predictive viewpoints. A simple picture to answer even basic questions, such as why the meander occurs and why this instability is oscillatory (i.e., a Hopf bifurcation) beyond numerical observation is missing. From a predictive viewpoint, we still lack a quantitative analytical understanding of what controls the ∂M boundary or the frequency ratio ω_2/ω_1 in the parameter space of reaction-diffusion models. Similar uncertainties are to a large extent also present for other phenomena like spiral drift under external action.

A kinematical model of spiral dynamics, aimed at the weakly excitable large core limit, has been proposed some years ago on a purely phenomenological basis [18]. It has been helpful to rationalize experimental facts but it has not been derived from the underlying reaction-diffusion equations. Thus it remains limited in its predictions, e.g., it falls short of predicting the ∂M boundary and the ratio ω_2/ω_1. Moreover, at a more conceptual level, the general validity of the boundary condition assumed for the free end of the wave front in this kinematic theory remains somewhat unclear.

The first goal of this paper is to present a rigorous asymptotic derivation of a kinematic theory of spiral wave motion in the weakly excitable and free-boundary limit (lower left hand corner of Fig. 1) on which we focus. As we shall see, the structure of this theory differs from the one proposed phenomenologically in Ref. [18]. The second goal of this paper is to demonstrate, through selected applications of this theory, that it is able to provide a physical and quantitative understanding of a wide range of wave phenomena such as meander, drift under various external actions considered in previous studies [19–25], and multiarm spiral wave motion. Highlights of our results include an asymptotically exact treatment of the meander instability for $\epsilon\ll 1$, which gives the precise location of the ∂M boundary and shows that the instability arises from a supercritical Hopf bifurcation with $\omega_2/\omega_1=1/2$ in this limit, the finding that multiarm spiral waves with two or more arms are always linearly unstable, in contrast to a previous numerical study [26], and predictions of the spiral drift speed and drift angle in an external field. These results are generally found to be in good quantitative agreement with our simulations of FN kinetics.

The starting point of our analysis is the standard free-boundary limit of reaction-diffusion models [27] described in Sec. II, which is valid when the excited region is surrounded by a thin interface of width $\epsilon\ll 1$. In this limit, the fast activator variable is eliminated in favor of an eikonal equation that gives the normal velocity of this boundary. This velocity generally depends on the local radius of curvature of this interface, assumed large compared to ϵ, as well as the local value of the slow controller variable at the interface.

This free-boundary problem is nontrivial to solve because it requires us to treat both the dynamics of the wave front, which is the part of the boundary where the excited region propagates into the recovery region of the medium, and the wave back where the reverse process occurs. Far from the tip, the front and back behave essentially identically, such that a ''single-front'' description is rigorously possible. In the tip region, however, the front and back must be matched at the tip (i.e., point of zero normal velocity along the boundary), which is a difficult task. For this reason a single-front description with a somewhat arbitrary tip condition was first used historically to relate the steady rotation frequency and core radius of spirals [28]. The kinematic theory of Ref. [18] is an attempt to extend this picture to an unsteady situation. Subsequent solutions of the complete free-boundary problem, with a rigorous matching of front and back that provides a unique and independent determination of the spiral frequency and wavelength, focused on two limits. One of these limits (see [29] and earlier references therein) is obtained mathematically by assuming $\epsilon\ll 1$ while keeping Δ fixed of order unity, which corresponds physically to a highly excitable medium. The wavelength and frequency obey in this limit [30] certain scaling laws with ϵ proposed by Fife [31]. The wave front and wave back, however, are matched onto

singular core solutions (of size ϵ with only activator diffusion) that have later been shown to be generically unstable [29]; this result actually seems to agree with the numerical observation of complex meander (and thus unstable motion) in this limit [12]. Thus these solutions do not provide a proper starting point for a kinematic theory aimed to describe the onset of meander. A better starting point, on which we focus here, is the second limit originating from Ref. [32] where one constructs smooth core solutions to the free-boundary problem. It was shown in [33] that this can in fact only be consistently done for a weakly excitable medium when the radius of curvature of the boundary at the tip remains much larger than the front and back interface width, i.e., by assuming simultaneously $\epsilon \ll 1$ and $\Delta \sim \epsilon^{1/3} \ll 1$. This allowed a rigorous derivation of the line ∂R in the weak excitability limit [33] in good quantitative agreement with numerical simulations of FitzHugh-Nagumo kinetics (lower left-hand corner of Fig. 1), as well as a semianalytic derivation of the selected core radius/frequency of spiral waves and retracting wave speed in the same limit [34].

The present kinematic theory is derived by first refining analytically the description of steady retraction and rotation in this weakly excitable limit (Sec. IV), and then extending it to an unsteady regime (Sec. V) for the nontrivial case of self-interacting spirals, i.e., where the wave tip motion is influenced by the average controller concentration left by the previous passage of the wave front. This allows us to derive an equation of motion for the wave tip that is then used to analyze meander in a linear and nonlinear regime (Sec. VI). Results of these two sections have been summarized in a previous short publication [35]. Further applications of the kinematic theory are then contained in subsequent sections that include spiral drift under various external actions without self-interaction (Sec. VII) and interacting multiarm spiral waves (Sec. VIII). Finally, corrections to the large core results are discussed in Sec. IX and several points are further analyzed in four appendixes. In addition, for clarity of exposition, we have found best to first give a simple physical picture of the kinematic theory and summarize the main results of its application in Sec. III. This section is purposely aimed to discuss this theory in terms of experimentally measurable quantities as well as to provide a guide to the rest of the paper.

II. REACTION-DIFFUSION MODEL AND FREE-BOUNDARY LIMIT

We consider the classic activator (u) controller (v) two-variable reaction-diffusion model of excitable media [10],

$$\partial_t u = D_u \nabla^2 u + f(u,v)/\tau_u, \tag{1}$$

$$\partial_t v = D_v \nabla^2 v + g(u,v)/\tau_v, \tag{2}$$

with a linearly stable rest state (u_0, v_0). We focus in this paper on the singly diffusive case $D_v = 0$, although we shall also briefly consider the slow controller diffusion limit $\gamma \equiv D_v/D_u \ll 1$ in Sec. VI. The u nullcline $[f(u,v)=0]$ is assumed to have the standard S shape in the (u,v) plane. A simple choice of FN kinetics that we use for the numerical simulations is $f(u,v) = 3u - u^3 - v$, $g(u,v) = u - \delta$ with the rest state $u_0 = \delta, v_0 = 3\delta - \delta^3$. It is convenient to rewrite Eqs. (1) and (2) in a standard dimensionless form by measuring time and length in units of τ_v and $(D_u \tau_v^2/\tau_u)^{1/2}$, respectively, which yields for the singly diffusive case

$$\partial_t u = \epsilon \nabla^2 u + f(u,v)/\epsilon, \tag{3}$$

$$\partial_t v = g(u,v), \tag{4}$$

where $\epsilon \equiv \tau_u/\tau_v$. We study this dimensionless form of the equations in the rest of this paper, except in the next section where we summarize the essential ingredients of the kinematic theory in dimensional units. For small ϵ, the excited region ($u \simeq \sqrt{3}$ with the previous choice) of a propagating wave is separated by a sharp boundary from the unexcited or recovering medium ($u \simeq -\sqrt{3}$ with the previous choice). The wave description can thus be reduced to determining the motion of this boundary (i.e., a free-boundary problem) [2,28,32]:

$$c_n = c(v) - \epsilon\kappa, \tag{5}$$

$$\partial_t v = g(u^{\pm}(v), v) \quad \text{in} \quad \mathcal{D}^{\pm}, \tag{6}$$

where c_n is the normal velocity of the interface separating the excited and recovery regions of the medium denoted by $\mathcal{D}^+$ and $\mathcal{D}^-$, respectively, κ is the local curvature of this interface, and $u^{\pm}(v)$ denotes the rightmost $(+)$ and leftmost $(-)$ branch of the u nullcline $[f(u,v)=0]$. The function $c(v)$ is entirely determined by Eq. (3) with v fixed. We measure the excitability of the medium, i.e., the threshold stimulus necessary to cause a response, by the parameter $\Delta \equiv v_s - v_0$, where v_s is the stall value of v at which $c(v_s) = 0$. The isolated pulse speed $c_0 \equiv c(v_0)$ is then a monotonously increasing function of Δ with $c_0 = \alpha\Delta$ for $\Delta \ll 1$ ($\alpha = 1/\sqrt{2}$ for our numerical choice). For values of v near v_s, Eq. (6) can be simplified even further to

$$\partial_t v = \begin{cases} 1/\tau_e & \text{in} \quad \mathcal{D}^+ \quad (7) \\ -(v - v_0)/\tau_R & \text{in} \quad \mathcal{D}^-, \quad (8) \end{cases}$$

where the activator time scale $\tau_e = 1/g(u^+(v_s), v_s)$ controls the pulse duration and the recovery time

$$\tau_R = \left. \frac{\partial_u f}{(\partial_u g \partial_v f - \partial_v g \partial_u f)} \right|_{u = u^-(v_s), v = v_s} \tag{9}$$

is the time scale over which the controller variable returns to its rest state after an excitation [for our numerical choice, $\tau_e = 1/(2\sqrt{3}), \tau_R = 6$].

III. PHYSICAL PICTURE OF KINEMATIC THEORY AND MAIN RESULTS

A. Retraction and rotation

In a typical chemical or biological excitable medium, many parameters (chemical or ionic concentrations, temperature, light, etc.), control the excitability of the medium. However, independently of the complexity of the medium, it is generally possible to construct a single dimensionless parameter [33,34]

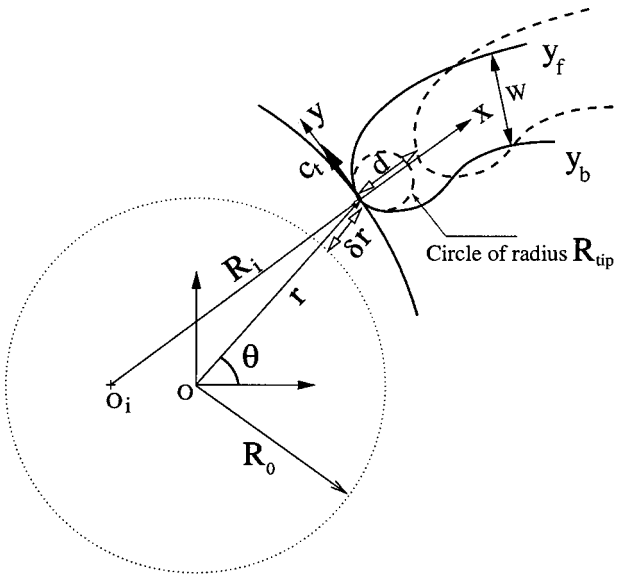

FIG. 3. Sketch of the spiral tip region and unsteady tip trajectory (solid lines). (r,θ) denotes the polar coordinates of the wave tip with respect to the fixed steady-state center of rotation O. R_i is the instantaneous radius of curvature of the unsteady tip trajectory about the instantaneous center of rotation O_i, with $O_i=O$ and $R_i=R_0$ for steady rotation, and $R_{\rm tip}$ is the radius of curvature of the boundary between the excited and recovery regions of the medium at the tip. c_t denotes the instantaneous tangential velocity of the wave tip along this trajectory, with $c_t=\omega_1 R_0$ for steady-state rotation. The coordinates $\delta r=r-R_0\equiv\epsilon q/c_0$ and $\psi=\theta-\omega_1 t$ measure the radial and angular departure from steady-state rotation, respectively. The Cartesian coordinate system (x,y) that moves with the wave tip is also shown with the y axis parallel to c_t. $y_f(x)$ and $y_b(x)$ denote the instantaneous wave-front and wave-back boundaries. Finally, $d=q(\theta)-q(\theta-2\pi)$ measures the radial displacement of the wave tip after one 2π rotation.

$$B=\frac{2R_{\rm tip}}{W}=\frac{2D_u}{c_0 W}, \tag{10}$$

which determines whether the tip rotates, and thus forms a spiral wave, or whether it simply retracts. This parameter is expressed as the ratio of two length scales that characterize the tip region of a broken plane wave that is shown schematically in Fig. 3. The first is the radius of curvature $R_{\rm tip}$ of the wave boundary at the tip. In the limit $(\epsilon\ll 1)$ where this boundary is thin, $R_{\rm tip}$ is obtained by applying the eikonal equation at the tip, which yields $c_n=0=c_0-D_u/R_{\rm tip}$, and thus $R_{\rm tip}=D_u/c_0$ where c_0 is the plane wave speed. The second length scale W is the constant width of the excited region away from the tip. As argued in [33,34], the wave boundary in the tip region can only be smooth if $R_{\rm tip}\sim W$, such that the ∂R boundary must correspond to a fixed value of $B=B_c$ of order unity; an explicit calculation (Refs. [33,34] and Sec. IV A here) yields $B_c=0.535$. For $B>B_c$, the excitability of the medium is not sufficient to overcome diffusion in the most highly curved part of the tip region, which retracts. In contrast for $B<B_c$, the excitability is sufficient to overcome retraction, and the increase of c_n away from the tip induces rotation.

Increasing (decreasing) B corresponds to decreasing (increasing) the excitability of the medium while moving normal to the ∂R boundary in the multidimensional parameter space that characterizes a given excitable medium. B is therefore the most natural parameter to characterize this excitability close to this boundary, and is used throughout this paper. From an experimental standpoint, c_0 and W are in principle measurable quantities and D_u can be either measured or estimated, such that one could attempt to quantify B directly. Of course, in practice, the definition of W, and thus B, becomes less precise when ϵ is not small and it is simpler to use an experimental control parameter $P_{\rm expt}$ (such as a concentration) that can be varied to cross the ∂R boundary. Therefore we will briefly describe in Sec. III C a more direct way to obtain a quantitative relationship between B and $P_{\rm expt}$ close to the ∂R boundary without the need to use Eq. (10).

B. Rigid wave tip and slaved wave front

Close to the ∂R boundary, we will show that a spiral wave in its tip region behaves as a ''rigid body'' whose motion can be characterized by giving two *instantaneous* quantities: the tip tangential velocity $c_t(t)$, and its rotation rate $\omega_i(t)=c_t(t)/R_i(t)$ where $R_i(t)$ is the radius of curvature of the tip trajectory as depicted in Fig. 3. Two key ingredients make this kinematic description possible. The first is that, near ∂R, the wave shape is close to a critical finger (i.e., the broken plane wave that simply translates without retraction or rotation for $B=B_c$) on a length scale $\ell\sim D_u/(c_0\sqrt{1-c_t/c_0})$ (as explained in Sec. IV C) that is large compared to the scale of the tip itself, $R_{\rm tip}=D_u/c_0$. The second is that the relations that govern c_t and R_i are established on time scales that are both much shorter than the steady rotation period, $T_0=2\pi/\omega_1$, as discussed at the start of Sec. V and in quantitative details in Appendix B. This separation of time scales, which makes our adiabatic treatment possible, becomes exact in the large core limit $B\to B_c$, but, importantly, it does not depend on ϵ being small. Therefore the present kinematic description should rigorously extend beyond the free-boundary limit but we shall assume that $\epsilon\ll 1$ in this paper to compute c_t.

A key difference between this description and the one proposed in [18] should already be apparent. Namely, here, the dynamics is driven entirely by the rigid tip region (which is just a point on the core scale). In contrast, in the kinematic model of [18], the tip motion is determined by the wave front dynamics via a boundary condition imposed at the tip. In the present context, the dynamics of the spiral wave-front outside the tip region *need not* be invoked to calculate the tip motion.

C. Tangential velocity

The tip tangential velocity is determined by the controller concentration (equivalently the spatial variation of excitability in which the wave front propagates) in the tip neighborhood. To compute this velocity we exploit the fact that, close to the ∂R boundary, the equations of motion can be linearized around the critical finger. This allows us to obtain a solvability condition (i.e., a general condition for the existence of a solution to these linearized equations) that uniquely relates the tangential velocity $c_t(\{v\})$ to an arbitrary spatial distribution of v; this distribution is only constrained to deviate slightly from the rest state v_0 in order for

the wave tip to remain close to the critical finger. This solvability condition is first used in Sec. IV B in the simplest steady-state situation where the tip propagates into a uniform controller concentration. The result of interest is

$$c_t/c_0 = 1 + (B - B_c)/K, \tag{11}$$

where $K \simeq 0.63$ is a numerical constant. This result implies that on the weak excitability side of the ∂R boundary ($B > B_c$), steady retracting waves form with $c_t/c_0 = \sqrt{c_r^2 + c_0^2}/c_0 > 1$, where c_r is the tip retracting speed. On the other side ($B < B_c$), spirals forms with $c_t/c_0 < 1$ and a second relation discussed in the next subsection is needed in this case to determine the rotation rate. The calculation of the tangential velocity is extended to the case of steady self-interacting spirals that propagate in a not fully recovered medium in Sec. IV D, to unsteady self-interacting spirals in Sec. V B, and to spirals in an external field in Sec. VII B. In the latter case, $c_t(\{v\}, E_\parallel, E_\perp)$ depends both on the controller concentration and the components $E_\parallel$ and $E_\perp$ of the external field, respectively, parallel and orthogonal to c_t.

A relation between B and an arbitrary experimental control parameter P_{expt} can be obtained close to the ∂R boundary by simply measuring the slope S of the curve c_t/c_0 vs P_{expt}, which should be the same on both sides of ∂R and presumably simpler to obtain on the retracting side. It then follows at once from Eq. (11) that

$$B - B_c = KS(P_{\text{expt}} - P_{\text{expt},c}) \tag{12}$$

close to ∂R, where $P_{\text{expt},c}$ is the value of P_{expt} where ∂R is crossed. This relationship can be used to relate quantitatively the results of the rest of this paper to experiments, keeping in mind that these results are only accurate asymptotically close to ∂R and for small ϵ.

D. Rotation rate

The motion of the wave tip region, although rigid, must generally be consistent with the motion of the rest of the wave front away from the tip. On the spiral side of ∂R, the tip region must necessarily rotate to accommodate the fact that its tip end translates at a slower speed than the plane waves radiated outward from the core (on the other side of ∂R, $c_t > c_0$ simply implies retraction of the tip). In Sec. IV C, we show that the tip and the far regions can be matched on the gently curved intermediate scale ℓ, yielding a rotation rate c_t/R_i, with

$$R_i = \frac{D_u}{c_0}\left[\frac{b}{(1 - c_t/c_0)}\right]^{3/2}, \tag{13}$$

where $b \simeq 2.946$ is a constant that is obtained by matching the curved tip and far regions. It should be noted that this constant differs from the constant b' [36] obtained by arbitrarily imposing a radial departure of the wave front from the steady-state circular core trajectory as in Ref. [18]. The 3/2 exponent, however, is the same both here and in Ref. [18] since it does not depend on details of the matching on the tip scale.

Equation (13) holds both for steady rotation (in the context of which it is derived in Sec. IV C) and for unsteady rotation owing to the aforementioned adiabatic approximation. For steady rotation, the core radius R_0 is simply obtained by substituting the expression for c_t from Eq. (11) into Eq. (13), which yields

$$R_0 = \frac{D_u}{c_0}\left[\frac{bK}{(B_c - B)}\right]^{3/2}. \tag{14}$$

The generalization to self-interacting spirals is given in Sec. IV D.

E. Parametrization of the wave tip trajectory

Knowing how to compute c_t and R_i gives in principle a complete kinematic theory of the wave tip motion, since this uniquely predicts the Euclidean trajectory of the tip in time. However, to characterize analytically the tip dynamics in unsteady situations (such as drift, meander, etc.) it is convenient to measure the instantaneous tip position by the standard polar coordinates (r, θ) with respect to a fixed origin at the center of steady rotation (Fig. 3), and to relate the tip motion in these coordinates to c_t and R_i. This part of our analysis is carried out in Sec. V A and yields a simple forced harmonic oscillator equation

$$\frac{d^2\delta r}{dt^2} + \omega_1^2 \delta r = \omega_1^2 \delta R_i, \tag{15}$$

where $\delta r(t) \equiv r(t) - R_0$ is the radial displacement of the wave tip from its radius R_0 of steady rotation and $\delta R_i(t) \equiv R_i(t) - R_0$. Equation (15) is valid for a small radial displacement ($|\delta r|/R_0 \ll 1$) and is accompanied by an independent equation for the angular displacement $\psi(t) \equiv \theta(t) - \omega_1 t$ from steady rotation. For a small radial displacement, however, the two equations are not coupled such that δr can be computed independently. Without forcing, the solution of Eq. (15), namely, a harmonic motion at frequency ω_1, is a simple superposition of the two translation modes: it gives the tip displacement of a steady spiral which is slightly translated with respect to the reference unperturbed spiral.

F. Main results

In summary, the application of the present kinematic theory contains three steps: (i) using a solvability condition to calculate c_t in terms of the local controller concentration, external field, etc., with a resulting expression that depends on the situation considered, (ii) using Eq. (13) to express R_i in terms of c_t, and (iii) solving Eq. (15) to obtain the radial displacement of the tip for a given forcing, which also obviously depends on the situation considered. We now summarize the result of this procedure for the selected applications examined in this paper (in a different order than in subsequent sections).

The simplest example (Sec. VII A) is to compute the tip motion induced by a small periodic spatially uniform variation of excitability $B(t) = B_0 + \delta B \sin(\omega_1 t + \phi)$. Following the above steps, and using the fact that the perturbation is small, we obtain at once

$$\frac{d^2\delta r}{dt^2}+\omega_1^2\delta r=\omega_1^2(dR_0/dB)\,\delta B\,\sin(\omega_1 t+\phi), \qquad (16)$$

where the function $R_0(B)$ is defined by Eq. (14), and dR_0/dB is to be evaluated at $B=B_0$. This resonant forced harmonic oscillator equation has a growing sinusoidal solution with an amplitude that increases linearly in time, and which thus corresponds to a spiral drift at a speed $c_d=\omega_1(dR_0/dB)\,\delta B/2$, or $c_d=\omega_1 dR_0/dP_{\rm expt}\delta P_{\rm expt}/2$ in an experiment. The action of an electric field is considered in Sec. VII B and produces a similar type of periodic forcing that leads to spiral drift. In agreement with previous studies [20,21,23–25] the spiral is found to drift at an angle with the external field. This result also determines the curvature-induced motion of a scroll filament. There the main prediction is that rings expand in the large core limit (i.e., the filament tension is negative) in agreement with previous numerical observations in this limit (see [37] and earlier references therein).

In the case of meander the tip tangential velocity and hence the forcing on the right-hand side of Eq. (15) depends on the radial displacement $\delta r(t)-\delta r(t-T_0)$ of the tip after one complete rotation (Fig. 3) due to the self-interaction of the wave front with its own recovery tail. If this displacement is positive, the average controller concentration will be slightly more elevated in the tip region (i.e., the medium will be slightly less excitable in this region) than if it is negative, which then affects $c_t(\{v\})$ and thus R_i and the forcing of the tip. This effect leads to a differential equation with delay of the form

$$\frac{d^2q}{dt^2}+\omega_1^2 q=\omega_1^2 mF(q(t)-q(t-T_0)), \qquad (17)$$

where we have defined the dimensionless radial displacement $q(t)=\delta r(t)/R_{\rm tip}=c_0\delta r(t)/D_u$, the parameter $m=3B_c(dR_0/dB)e^{-T_0/\tau_R}$, and F is a tanh-shaped function which we compute in Sec. V B. The saturation of F at large radial displacement is due to the fact that the controller concentration only varies appreciably on the scale of $R_{\rm tip}$. A linear stability analysis of this equation in Sec. VI A yields that the onset of meander occurs when m exceeds a threshold $3/[8F'(0)]$ that depends in a singular way on the diffusivity ratio D_v/D_u and ϵ. Namely, the function F is nonanalytic at 0 in the pure sharp boundary limit, Eqs. (5), (6) of the singly diffusive model, which sheds some light on difficulties that were previously encountered when attempting to perform a linear stability analysis in this limit [38]. However, for a finite interface width $\sqrt{D_u\tau_u}$, small compared to the spiral tip radius D_u/c_0, the slope at the origin is finite, with $F'(0)\sim-\ln(c_0\sqrt{\tau_u/D_u})$, such that there is a finite meander threshold that will be typically of order unity in experiments or simulations. In addition, this analysis predicts that $\omega_2/\omega_1=1/2$ at onset in the large core limit and a simple physical interpretation of both the existence of a threshold and oscillatory motion is given at the end of Sec. VI A. Slightly away from the large core limit, the discussion in Sec. IX leads to a modified differential equation with delay that shows that ω_2/ω_1 increases above 1/2 as the core radius R_0 is decreased, in semiquantitative agreement with numerical simulations. This actually provides a simple picture of the onset of quasiperiodicity (i.e., how ω_2/ω_1 becomes irrational) as one moves away from the large core limit.

Finally, for spirals with N arms, we obtain a system of N coupled differential equations with delay and with the interaction between the arms controlled by the parameter $m_N=3B_c(dR_0/dB)e^{-T_0/(N\tau_R)}$. An exact linear stability analysis shows that, unlike for meander, there is no finite threshold of instability. Moreover, this instability develops on a time scale proportional to $1/m_2^2$ for $N=2$ and $1/m_N$ for $N>2$, such that the time necessary to observe it grows exponentially as the ∂R boundary is approached.

IV. STEADY STATES

We start by analyzing steady wave patterns of the free-boundary problem (5)–(7). As shown in Refs. [32,33], when excitability is decreased, the spiral core radius and spiral period diverge on the line ∂R with $\Delta=\Delta_c(\epsilon)$ which marks the lower excitability limit of spiral wave propagation in the (ϵ,Δ) plane. As described in Sec. I, on the line ∂R, spirals degenerate into critical fingers that translate at c_0, the plane wave speed. For $\Delta<\Delta_c(\epsilon)$, the steady waves are retracting fingers. Laws for the tip retraction speed and spiral tip divergence were obtained in Ref. [34] from numerical computations in the neighborhood of the line $\Delta_c(\epsilon)$ for $\epsilon\ll 1$. Here, we begin by recalling the result of [33] about the line of existence of critical fingers. We then proceed and study steady patterns in the neighborhood of $\Delta_c(\epsilon)$ by perturbation around the critical fingers. On the retracting wave side, we determine the tangential speed of the tip as a function of $\Delta-\Delta_c(\epsilon)$ by a solvability condition [39]. This is the simplest example of the method that we will use in more complicated situations to determine the tip tangential speed. For $\Delta>\Delta_c(\epsilon)$, the critical finger winds up around its tip and becomes a steady spiral rotating around a circular core R_0 at a constant tangential speed c_t. We first consider the case where R_0 is large enough so that the spiral front interface can be assumed to propagate in the medium rest state (i.e., the disturbance of the medium induced by the tip previous passage can be neglected). We obtain analytically the divergence of the spiral radius by adding to the previous determination of c_t an analysis of the Burton-Cabrera-Frank (BCF) equation [40] in the large radius limit using matched asymptotics, thus confirming the laws obtained in Ref. [34]. Finally, we determine the modification of the steady spiral parameters induced by the perturbation of the medium characteristics due to previous passages of the spiral.

A. The line $\Delta_c(\epsilon)$ of critical fingers

We first examine the critical fingers that propagate in a shape preserving way at the pulse speed c_0 on the boundary $\Delta_c(\epsilon)$ in the parameter space (Δ,ϵ). For a small medium excitability, the scaling of the line $\Delta_c(\epsilon)$ is easily determined by comparing two length scales [33] as reviewed in Sec. III A. First, the condition that the normal velocity vanishes at the wave tip requires that the tip radius of curvature is equal to ϵ/c_0. This gives the order of magnitude of the distance between the wave front and wave back. Second, the front and back interfaces should move at the same velocity. The value

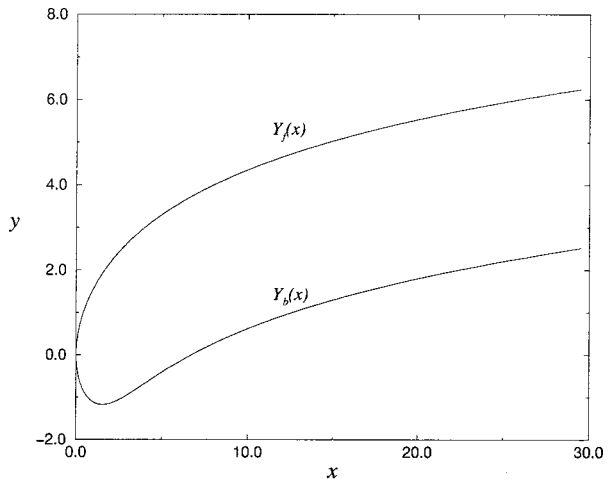

FIG. 4. The critical finger: the solution of Eqs. (18) and (19) for $B=B_c$.

of the controller field v should therefore increase from $v_0=v_s-\Delta$ on the front interface to $v_s+\Delta$ on the back interface in a time $(\epsilon/c_0)/c_0$. This gives $\tau_e\epsilon/c_0^2\sim\Delta$ and, remembering that $c_0=\alpha\Delta$, the scaling $\Delta_c(\epsilon)\sim(\epsilon/\alpha^2\tau_e)^{1/3}$.

A more detailed analysis is required to determine the constant in this asymptotic relation and the critical finger shape that we will subsequently need. We follow Ref. [33] and search for a steady-state finger shape translating at c_0, the isolated pulse speed. It is convenient to work in the frame of the finger with the origin at the finger tip (see Fig. 4) and to use as length unit ϵ/c_0, the finger tip radius. On the front interface $Y_f(x)$, the value of the controller field is equal to the rest state value v_0. At point x on the back interface, the controller field value has increased to $v_0+\epsilon[Y_f(x)-Y_b(x)]/c_0^2\tau_e$ from Eq. (8). Equation (5) therefore implies that

$$\frac{d^2Y_f}{dx^2}=\left[1+\left(\frac{dY_f}{dx}\right)^2\right]-\left[1+\left(\frac{dY_f}{dx}\right)^2\right]^{3/2}, \tag{18}$$

$$\frac{d^2Y_b}{dx^2}=\left[1+\left(\frac{dY_b}{dx}\right)^2\right]+\{1-B[Y_f(x)-Y_b(x)]\}\times\left[1+\left(\frac{dY_b}{dx}\right)^2\right]^{3/2}, \tag{19}$$

where $Y_f(x)$ denotes the front interface of the finger and $Y_b(x)$ its back interface. These equations depend on the single parameter $B=\epsilon/(\alpha^2\tau_e\Delta^3)$ [41]. The desired solutions should satisfy at the tip the boundary conditions $Y_f(0)=Y_b(0)=0$, $dY_f/dx(0)=-dY_b/dx(0)=+\infty$, and asymptotically $dY_f/dx(+\infty)=dY_b/dx(+\infty)=0$.

The solution of Eq. (18) does not require any supplementary condition. At $x=0$, it tends to zero as $Y_f(x)\sim\sqrt{2x}$ in agreement with the chosen tip radius of length unity. At $x=+\infty$, it diverges logarithmically, $Y_f(x)\sim 2\ln(x)$. In fact, $Y_f(x)$ can be obtained analytically,

$$x=2\arctan(v)+\frac{2}{v-1}-\pi,$$

$$Y_f=\ln\left[\frac{v^2+1}{(v-1)^2}\right], \tag{20}$$

with $1\leqslant v<+\infty$.

On the contrary, Eq. (19) can be solved with the appropriate boundary conditions only for a particular value of the parameter B. The two boundary conditions at $x=0$ entirely determine the solution of Eq. (19) once the front interface is determined. The solution $Y_b(x)$ should approach $[Y_f(x)-2/B]$ as $x\to+\infty$ to satisfy the boundary condition at infinity. A linearization of Eq. (19) around this asymptotic behavior gives a convergent mode and a divergent mode growing as $\exp(\sqrt{B}x)$. So, the solution obeys the right boundary condition at $x=+\infty$ only for the special values of B which cancel the prefactor of the diverging mode. This is numerically found to happen for $B_c=0.5353\ldots$ which defines the line of existence $\Delta_c(\epsilon)$ of the critical fingers in the (ϵ,Δ) plane. In the following, we refer to the solution of Eqs. (18) and (19) with $B=B_c$ as the ''critical finger shape.'' It is plotted in Fig. 4.

Remark. One can note that at the level of Eqs. (18) and (19) the interface is continuous and so are its first two derivatives. However, its third derivative is discontinuous at the finger tip $(x=0,y=0)$ since one has $Y_f(x)=\sqrt{2x}+x/3+\cdots$ while $Y_b(x)=-\sqrt{2x}+x(1-2B_c)/3+\cdots$ (and $B_c\neq 0$). This weak nonanalyticity can be cured by introducing a small boundary layer near the tip as discussed in Appendix A.

B. Retracting fingers

We consider a medium characterized by a parameter $B=\epsilon/(\alpha^2\tau_e\Delta^3)$ higher than B_c, that is, not excitable enough to allow for the existence of spirals. We look for steady-state shapes propagating at c_t. We use as before ϵ/c_0 as unit length where $c_0=\alpha\Delta$ is the velocity of the planar front in the considered medium. Equations (5) determining the front y_f and back y_b interfaces become

$$\frac{d^2y_f}{dx^2}=\frac{c_t}{c_0}\left[1+\left(\frac{dy_f}{dx}\right)^2\right]-\left[1+\left(\frac{dy_f}{dx}\right)^2\right]^{3/2}, \tag{21}$$

$$\frac{d^2y_b}{dx^2}=\frac{c_t}{c_0}\left[1+\left(\frac{dy_b}{dx}\right)^2\right]+\left[1-B\frac{c_0}{c_t}[y_f(x)-y_b(x)]\right]\times\left[1+\left(\frac{dy_b}{dx}\right)^2\right]^{3/2}. \tag{22}$$

The solutions should satisfy at the tip the same boundary conditions as the critical fingers, $y_f(0)=y_b(0)=0$, $dy_f/dx(0)=-dy_b/dx(0)=+\infty$. Asymptotically, they should obey $dy_f/dx(+\infty)=dy_b/dx(+\infty)=\sqrt{(c_t/c_0)^2-1}$. As for the critical finger, the solution of Eq. (21) for the front interface can be obtained for any value of the ratio $U=c_t/c_0>1$ and is given by

$$x=\frac{2}{U}\arctan(v)-\frac{1}{U\sqrt{U^2-1}}\ln\left(\frac{v-U-\sqrt{U^2-1}}{v-U+\sqrt{U^2-1}}\right)-\frac{\pi}{U},$$

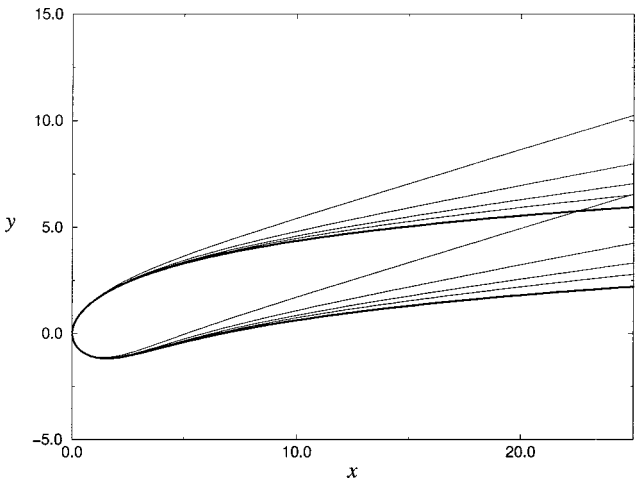

FIG. 5. Several retracting fingers ($U=1.05,1.02,1.01,1.005$ and corresponding values of $B=0.5669,0.5479,0.5416,0.538\,48$) compared to the critical finger (bold line).

$$y_f=\frac{1}{U}\ln\left[\frac{v^2+1}{v^2+1-2Uv}\right], \tag{23}$$

with $U+\sqrt{U^2-1}<v<+\infty$. On the contrary, Eq. (22) for the back interface can be solved with the correct boundary condition only if B is chosen appropriately for each value of U. Several obtained shapes are shown in Fig. 5. In Ref. [34], the solution of Eq. (22) was computed in such a way for several values of U close to one and it was found that c_t/c_0 extrapolates linearly to one when $B\to B_c$,

$$\frac{c_t}{c_0}=1+\frac{B-B_c}{K}, \tag{24}$$

with the constant $K\simeq 0.63$.

We show how the result (24) can be derived by analyzing perturbatively Eqs. (21), (22) around the critical finger [39]. For $|c_t/c_0-1|\ll 1$, the front interface of the retracting finger y_f is close to the front interface of the critical finger Y_f on distances of the finger tip small compared to $(c_t/c_0-1)^{-1/2}$. In this region, we linearize Eqs. (21), (22) around the critical finger shape as $y_f=Y_f+\delta y_f, y_b=Y_b+\delta y_b$. The corrections $\delta y_f, \delta y_b$ obey the inhomogeneous linear equations

$$\mathcal{L}_f(\delta y_f)=\frac{\delta c_t}{c_0}\left[1+\left(\frac{dY_f}{dx}\right)^2\right], \tag{25}$$

$$\mathcal{L}_b(\delta y_b)=\frac{\delta c_t}{c_0}\left[1+\left(\frac{dY_b}{dx}\right)^2\right]+\left[\left(B_c\frac{\delta c_t}{c_0}-\delta B\right)\times[Y_f(x)-Y_b(x)]-B_c\delta y_f\right]\left[1+\left(\frac{dY_b}{dx}\right)^2\right]^{3/2}. \tag{26}$$

We have introduced $\delta B=B-B_c, \delta c_t=c_t-c_0$ and the linear operators $\mathcal{L}_f, \mathcal{L}_b$ which are given by

$$\mathcal{L}_f=\frac{d^2}{dx^2}+\left\{-2+3\left[1+\left(\frac{dY_f}{dx}\right)^2\right]^{1/2}\right\}\frac{dY_f}{dx}\frac{d}{dx}, \tag{27}$$

$$\mathcal{L}_b=\frac{d^2}{dx^2}-a(x)\frac{d}{dx}-b(x), \tag{28}$$

with

$$a(x)=\left\{2+3\{1-B_c[Y_f(x)-Y_b(x)]\}\times\left[1+\left(\frac{dY_b}{dx}\right)^2\right]^{1/2}\right\}\frac{dY_b}{dx},$$

$$b(x)=B_c\left[1+\left(\frac{dY_b}{dx}\right)^2\right]^{3/2}. \tag{29}$$

The boundary values at the tip are $\delta y_f(0)=\delta y_b(0)=0$. For the derivatives, one obtains, using the asymptotic behavior $Y_f(x)\sim -Y_b(x)\sim\sqrt{2x}$ near $x=0$,

$$\left.\frac{d\delta y_f}{dx}\right|_{x=0}=\frac{1}{3}\frac{\delta c_t}{c_0}, \tag{30}$$

$$\left.\frac{d\delta y_b}{dx}\right|_{x=0}=\frac{1}{3}\left[\frac{\delta c_t}{c_0}(1+2B_c)-2\delta B\right]. \tag{31}$$

As before, Eq. (25) can be integrated and one obtains $\delta y_f=\eta_1\delta c_t/c_0$ where η_1 is the solution of

$$\mathcal{L}_f(\eta_1)=1+\left(\frac{dY_f}{dx}\right)^2, \tag{32}$$

such that $\eta_1(0)=0, \eta_1'(0)=1/3$. When $x\to+\infty$, η_1 grows like $x^2/6$. The situation is different for Eq. (26). For large x, $\mathcal{L}_b$ reduces to d^2/dx^2-B_c. So, in general, δy_b grows exponentially as $\exp(\sqrt{B_c}x)$ on distances of order one much smaller than the region where the linearized equation (26) is valid. It is only when $\delta c_t/c_0$ is related in a particular way to δB that the exponential growth is absent and that δy_b can grow algebraically like δy_f, as it should. In order to determine the relation between $\delta c_t/c_0$ and δB that should be imposed, we find it convenient to introduce the zero mode $\xi(x)$ of the adjoint $\mathcal{L}_b^\dagger$ which vanishes (exponentially) at infinity,

$$\mathcal{L}_b^\dagger(\xi)=\frac{d^2\xi}{dx^2}+\frac{d}{dx}[a(x)\xi]-b(x)\xi=0,\ \xi(+\infty)=0, \tag{33}$$

where the functions $a(x)$ and $b(x)$ are defined by Eq. (29). ξ is uniquely defined up to a global normalization. A local analysis shows that ξ automatically vanishes at $x=0$ and that it tends linearly to zero when $x\to 0$. For definiteness, we normalize $\xi(x)$ so that its maximum value is equal to 1. A graph of ξ is shown in Fig. 6. We now multiply both sides of Eq. (26) by $\xi(x)$ and integrate over x from x_1 to x_2. Integration by parts gives for the left-hand side

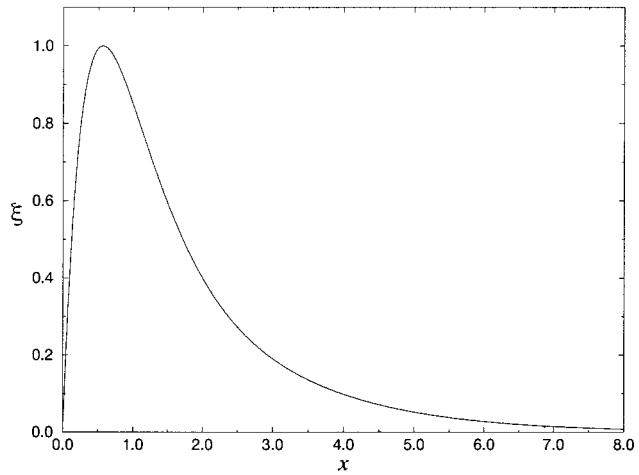

FIG. 6. Graph of the zero mode $\xi(x)$ of the operator $\mathcal{L}_b^\dagger$ normalized by imposing that the maximum value of $\xi(x)$ is one.

$$\int_{x_1}^{x_2} dx\,\xi(x)\mathcal{L}_b(\delta y_b)=\left[\xi\frac{d\delta y_b}{dx}-\delta y_b\frac{d\xi}{dx}-a(x)\xi(x)\delta y_b\right]_{x_1}^{x_2}+\int_{x_1}^{x_2} dx\,\delta y_b(x)\mathcal{L}_b^\dagger(\xi). \tag{34}$$

The integral on the left-hand side of Eq. (34) vanishes since $\mathcal{L}_b^\dagger$ annihilates ξ, Eq. (33). Moreover, when $x_1\to 0$ and $x_2\to+\infty$ the boundary terms also vanish when δy_b satisfies the correct boundary condition. Terms at $x=+\infty$ vanish when δy_b grows algebraically since $\xi(x)$ vanishes exponentially. There is no contribution at zero since δy_b and $\xi(x)$ vanish linearly, which compensates for the singular behavior of $a(x)=-3/(2x)+\cdots$. Therefore, the right-hand side of Eq. (26) has to satisfy the solvability condition,

$$\frac{\delta c_t}{c_0}[I_1+B_c(-I_2+I_3)]-\delta B I_3=0, \tag{35}$$

where the constants I_1, I_2, I_3 are given by the following integrals which have been numerically evaluated:

$$I_1=\int_0^{+\infty} dx\,\xi(x)\left[1+\left(\frac{dY_b}{dx}\right)^2\right]\simeq 2.771,$$

$$I_2=\int_0^{+\infty} dx\,\xi(x)\,\eta_1(x)\left[1+\left(\frac{dY_b}{dx}\right)^2\right]^{3/2}\simeq 3.814,$$

$$I_3=\int_0^{+\infty} dx\,\xi(x)[Y_f(x)-Y_b(x)]\left[1+\left(\frac{dY_b}{dx}\right)^2\right]^{3/2}\simeq 7.708. \tag{36}$$

Equation (35) shows that the tangential velocity of the retracting finger tip depends linearly on the departure of B from B_c as stated in Eq. (24). The proportionality constant K is in excellent agreement with the value obtained by numerical extrapolation in Ref. [34].

$$K=B_c+(I_1-B_cI_2)/I_3\simeq 0.630. \tag{37}$$

Note that the values (36) of the integrals depend on the normalization of ξ but that the expression of the physical constant K appears as a ratio of such integrals and is thus independent of this (arbitrarily chosen) normalization. It is also important to remark that Eq. (35) shows that the tangential tip velocity is an appropriate quantity for a perturbative calculation around ∂R since it has a smooth behavior when ∂R is crossed. This should be contrasted with the retracting tip velocity which decreases as the square root of the distance to ∂R on the retraction side and does not appear to have a simple continuation on the spiral side of ∂R.

C. Steadily rotating spirals

For $B=\epsilon/(\alpha^2\tau_e\Delta^3)<B_c$, steady spiral waves exist. Their tip rotates around a circular core R_0 at a constant tangential tip velocity $c_t=\omega_1 R_0$. When $B\to B_c$, R_0 diverges, $c_t\to c_0$, and the tip of the spiral becomes closer and closer to a critical finger. In this subsection, we determine R_0 and ω_1 as a function of B (''the excitability of the medium''). We begin by considering spirals of radius large enough so that one can neglect the disturbance of the medium due to the spiral previous passage. In this case, the front interface can be assumed to propagate in the medium rest state. The spiral shape is analyzed by decomposing it into three overlapping regions where different approximations can be performed. Close to the tip, on distances of order $R_{\rm tip}=\epsilon/c_0$, the curvature of the tip trajectory can be neglected and a transposition of the analysis of the preceding subsection shows that the tangential velocity is linearly related to $\delta B=B-B_c$ by Eq. (24), namely, $\delta c_t=\delta B/K$ (both sides being negative now). Far from the tip, it is the effect of the interface curvature on the normal velocity [Eq. (5)] which can be neglected. The normal velocity can be taken constant, equal to c_0 and the spiral shape is then simply determined. These two approximate descriptions match at a distance of order ℓ from the spiral tip in an intermediate region where the interface is almost normal to the tip circle of rotation and the interface curvature is small. The intermediate scale ℓ appears as the balance between two effects. On one hand, the tip tangential velocity is smaller than c_0 by about $\omega_1\ell$ for purely kinematical reasons so that $|\delta c_t|\sim c_0\ell/R_0$. On the other hand, ℓ is the distance where curvature effects become small enough to be comparable to this velocity drop. At a distance ℓ from its tip, the critical finger curvature is of the order $2R_{\rm tip}/\ell^2$. This provides the alternative estimate $|\delta c_t|\sim\epsilon R_{\rm tip}/\ell^2$. Comparing both expressions and remembering that $R_{\rm tip}=\epsilon/c_0$ gives $\ell\sim(R_{\rm tip}^2R_0)^{1/3}$ and $|\delta c_t/c_0|\sim(R_{\rm tip}/R_0)^{2/3}$. The detailed analysis reported below replaces this simple order of magnitude estimate by the precise asymptotic relation,

$$\frac{c_0-c_t}{c_0}\simeq b\left(\frac{R_{\rm tip}}{R_0}\right)^{2/3}, \tag{38}$$

where the numerical constant b is obtained from the first zero a_1 of Airy function Ai [42], $b=-2^{1/3}a_1\simeq 2.946$ [36]. Comparing Eq. (38) with Eq. (24) determines the frequencies and core radii of steady spirals near the line $\Delta_c(\epsilon)$,

$$R_0=R_{\rm tip}\left(\frac{bK}{B_c-B}\right)^{3/2},\quad \omega_1=\frac{c_0}{R_{\rm tip}}\left(\frac{B_c-B}{bK}\right)^{3/2}. \tag{39}$$

1. Front interface

We first consider the front interface and assume that the spiral propagates in the medium rest state (this is of course justified only if the spiral period is long enough and it is required to be sufficiently close to the line ∂R). The equation for the front spiral interface is then identical to the classic equation for the growth of screw dislocations on crystal surfaces [40]. For a steady rotation at frequency ω_1 in a counterclockwise direction, Eq. (5) gives for the front spiral interface in polar coordinates (r,θ)

$$r\omega_1 = c_0\left[1+\left(r\frac{d\theta_f}{dr}\right)^2\right]^{1/2} + \epsilon\left(\frac{d\theta_f}{dr}+\frac{(d/dr)(rd\theta_f/dr)}{1+(rd\theta_f/dr)^2}\right), \tag{40}$$

with the boundary condition at infinity $d\theta_f/dr \to -\omega_1/c_0$. Rescaling coordinates makes it clear that Eq. (40) depends on the single dimensionless parameter $\Omega = \omega_1\epsilon/c_0^2$. For $0 < \Omega < 0.331$, it is found that $d\theta_f/dr \to +\infty$ at $r = R_0$ when Eq. (40) is integrated from $r = +\infty$. R_0 is the location of the spiral tip and is found to increase from 0 to $+\infty$ when Ω decreases from 0.331 to 0. The limit $\Omega \to 0.331$ has been considered in previous works [29,30]. We focus here on the other limit $\Omega \to 0$ where the excited region width ($\sim \epsilon/c_0$) becomes much smaller than the core radius ($\sim c_0/\omega_1$). In this limit, the front spiral interface can be separated into three distinct regions.

(1) Far from the spiral tip (the outer region), the interface scale of variation is c_0/ω_1. Introducing the rescaled coordinates $r = zc_0/\omega_1$ shows that the terms involving the interface curvature are multiplied by the small parameter Ω. Neglecting them, Eq. (40) becomes

$$z\frac{d\theta_{\text{out}}}{dz} = -\sqrt{z^2-1}, \tag{41}$$

which is of course integrable. This first approximation breaks down near $z = 1$, where the solution of Eq. (41) has a fast variation on the z scale and the formally negligible terms are important.

(2) Close to the spiral tip, Eq. (40) can be simplified in a different way. One can introduce the radial distance x from the tip circle of rotation measured in unit of the tip radius such that $r = R_0 + \epsilon/c_0 x$ and the tangential displacement $y\epsilon/c_0 = R_0\theta_f$. At lowest order in $\epsilon/(c_0R_0)$, Eq. (40) becomes identical in these variables to Eq. (18) for the front interface of a critical finger.

(3) These two different descriptions do not directly match. The transition occurs in an intermediate region where the interface curvature is small and the interface tangent almost radial. We thus assume (and check *a posteriori*) that dy/dx is small and expand the square root and denominator in Eq. (40). This gives

$$\frac{c_t - c_0}{c_0} + \frac{\epsilon}{c_0R_0}x = \frac{1}{2}\left(\frac{dy}{dx}\right)^2 + \frac{d^2y}{dx^2}, \tag{42}$$

where the tangential tip velocity $c_t = R_0\omega$ has been introduced. The different terms of Eq. (42) are of comparable magnitude for $x \sim (R_0c_0/\epsilon)^{1/3}, dy/dx \sim (\epsilon/R_0c_0)^{1/3}$, and $c_t/c_0 - 1 \sim (\epsilon/R_0c_0)^{2/3}$. In the limit $R_{\text{tip}} = \epsilon/c_0 \ll R_0$, this justifies the expansion leading to Eq. (42) and the neglect of higher-order terms. Introducing the rescaled variable $\xi = x[\epsilon/(2c_0R_0)]^{1/3}$, Eq. (42) becomes

$$\frac{1}{2}\frac{d^2y}{d\xi^2} + \frac{1}{4}\left(\frac{dy}{d\xi}\right)^2 = \xi + a_1, \tag{43}$$

where we have defined

$$a_1 = 2^{-1/3}\left(\frac{c_0R_0}{\epsilon}\right)^{2/3}\frac{c_t - c_0}{c_0}. \tag{44}$$

The Riccati equation (43) can be transformed into the linear Airy equation. Matching with Eq. (41) imposes that $dy/d\xi < 0$ when $\xi \to +\infty$. This imposes that the Airy function decreases at infinity and is proportional to Ai [42]. It gives $dy/d\xi = 2A_i'(\xi + a_1)/A_i(\xi + a_1)$. Using the asymptotic behavior [42] $\text{Ai}(\xi) \sim 1/2\pi^{-1/2}\xi^{-1/4}\exp(-2/3\xi^{3/2})$, one indeed checks that the obtained large ξ behavior $dy/d\xi \sim -2\sqrt{\xi}$ coincides with the behavior of Eq. (41) near $z = 1$. Matching with the tip region requires that the small ξ behavior of $dy/d\xi$ coincides with the asymptotic behavior of Eq. (18) when $x \to +\infty$, namely, $dy/dx \sim 2/x^2$. This requires a_1 to be a zero of Ai. Since $y(\xi)$ should be well defined for all real positive ξ it is necessarily the first one, $a_1 = -2.3381\ldots$ [42]. Comparing with the definition (44) of a_1 directly leads to the relation (38).

The relation $\omega_1(R_0)$, numerically determined in [43], was approximately obtained in [18,28] by assuming a radial departure of the front interface imposed on a fictitious inner radius R_0. This boundary condition is equivalent to requiring that θ be maximum at R_0. It is worth noting that, in the present limit, it would simply amount to replacing the exact value of the constant a_1 by the location of the maximum of Ai, namely, $a_1' = -1.018\,79\ldots$ [42]. Correspondingly, this would replace the exact value $b \simeq 2.946$ in Eq. (38) by $b' \simeq 1.283$.

2. The back interface

The equation for the back interface reads, in polar coordinates,

$$r\omega_1 = \left(-c_0 + \frac{\alpha}{\omega_1\tau_e}(\theta_f - \theta_b)\right)\left[1+\left(r\frac{d\theta_b}{dr}\right)^2\right]^{1/2} + \epsilon\left(\frac{d\theta_b}{dr}+\frac{(d/dr)(rd\theta_b/dr)}{1+(rd\theta_b/dr)^2}\right). \tag{45}$$

As for the front interface, we proceed by separately analyzing three regions. We consider first the tip region which plays the dominant role here. Introducing as before the coordinates x and y such that $r = R_0 + \epsilon/c_0 x, y\epsilon/c_0 = R_0\theta_b$, Eq. (45) becomes at lowest order in ϵ/c_0R_0 identical to Eq. (22) describing the back interface of retracting fingers (except that now $c_t < c_0$ and $B < B_c$). As in this previous case, requiring that the back interface does not diverge exponentially from the front interface relates c_t/c_0 to B. For B close to B_c, one can linearize around the critical finger and follow the previous analysis (25)–(37) which leads to Eq. (24). The compari-

son of Eqs. (24) and (38) gives the expression (39) for the spiral core radius and frequency of rotation as a function of B.

As one moves away from the tip, the back Y_b of the critical finger relaxes exponentially toward $Y_f - 2/B_c$ on the scale of the finger tip width. The equations describing the back and front interfaces are thus essentially identical in the intermediate and far regions and the analysis of Sec. IV C 1 applies as well to the back equation.

D. Steady self-interacting spirals

The analysis of the preceding section applies when the spiral period $T_0 = 2\pi/\omega_1$ is long enough compared to the recovery time constant τ_R so that the front interface can be assumed to propagate in the medium rest state. This applies for Δ sufficiently close to $\Delta_c(\epsilon)$ but as the medium excitability increases the spiral radius decreases and the front interface begins to feel the medium disturbance due to the spiral previous passages. This eventually leads to spiral meander as we show in the next section. As a preliminary step, we analyze here the influence of this medium modification on the steady spiral parameters R_0 and ω_1.

The concentration of the controller v on the front and back interfaces follows from Eqs. (8) and (7). For a spiral rotating steadily at frequency ω_1 in a counterclockwise direction, they are given by

$$v_f(r) = v_0 + \delta v_f(r), \tag{46}$$

$$v_b(r) = v_f(r) + \frac{\theta_f(r) - \theta_b(r)}{\omega_1 \tau_e}, \tag{47}$$

with

$$\delta v_f(r) = \frac{\theta_f(r) - \theta_b(r)}{\omega_1 \tau_e} \times \frac{\exp\{-[2\pi + \theta_b(r) - \theta_f(r)]/\omega_1 \tau_R\}}{1 - \exp\{-[2\pi + \theta_b(r) - \theta_f(r)]/\omega_1 \tau_R\}}. \tag{48}$$

Near the line $\Delta_c(\epsilon)$, ω_1 tends to zero, $\delta v_f(r)$ becomes negligible, and the concentration of v on the front interface can be taken equal to v_0 as done in the preceding subsection. This approximation is justified as long as δv_f induces a change in the front velocity which is negligible compared to the difference $c_t - c_0$ between the tip velocity and c_0. That is, for $\exp(-2\pi R_0/c_0\tau_R) \ll \delta c_t/c_0$ or using the estimate (39), $\exp[-2\pi R_{\rm tip}/c_0(bK/B_c - B)^{3/2}] \ll B_c - B$. Therefore, one can neglect the perturbation of the medium as long as $B_c - B \ll \epsilon^{2/9}$ (up to logarithmic corrections) or equivalently $\Delta - \Delta_c \ll \epsilon^{5/9}$. The results (39) are modified when $\delta v_f(r)$ becomes comparable to δc_t. The transition regime where $\delta v_f(r)$ is still small can be analyzed along the lines of the previous subsections,

$$r\omega_1 = c[v_0 + \delta v_f(r)]\left[1 + \left(r\frac{d\theta_f}{dr}\right)^2\right]^{1/2} + \epsilon\left(\frac{d\theta_f}{dr} + \frac{(d/dr)(rd\theta_f/dr)}{1 + (rd\theta_f/dr)^2}\right), \tag{49}$$

$$r\omega_1 = -c[v_b(r)]\left[1 + \left(r\frac{d\theta_b}{dr}\right)^2\right]^{1/2} + \epsilon\left(\frac{d\theta_b}{dr} + \frac{(d/dr)(rd\theta_b/dr)}{1 + (rd\theta_b/dr)^2}\right). \tag{50}$$

In the tip region, it is useful to introduce as previously the coordinates x and y, with $r = R_0 + \epsilon/c_0 x, y\epsilon/c_0 = R_0\theta$. At lowest order in $\epsilon/(c_0 R_0)$, Eq. (49) becomes

$$\frac{d^2 y_f}{dx^2} = \frac{c_t}{c_0}\left[1 + \left(\frac{dy_f}{dx}\right)^2\right] - \left[1 - \frac{\alpha}{c_0}\delta v_f(r)\right]\left[1 + \left(\frac{dy_f}{dx}\right)^2\right]^{3/2}. \tag{51}$$

We are interested in the parameter region where $\alpha\delta v_f(r)/c_0$ is of the same order as $\delta c_t/c_0$. As found above, this happens when the spiral period is large but only logarithmically in ϵ. This allows us to expand the exponential in Eq. (48) and to obtain the expression of the medium perturbation as a function of the critical finger shape,

$$\frac{\alpha}{c_0}\delta v_f(r) = B_c[Y_f(x) - Y_b(x)]\exp\left(-\frac{2\pi R_0}{c_0\tau_R}\right). \tag{52}$$

We expand the spiral front in the tip region around the critical finger shape as $y_f(x) = Y_f(x) + \delta y_f(x)$. The correction $\delta y_f(x)$ obeys the equation

$$\mathcal{L}_f(\delta y_f) = \frac{\delta c_t}{c_0}\left[1 + \left(\frac{dY_f}{dx}\right)^2\right] + B_c e^{-2\pi R_0/c_0\tau_R} \times [Y_f(x) - Y_b(x)]\left[1 + \left(\frac{dY_f}{dx}\right)^2\right]^{3/2}, \tag{53}$$

where the linear operator $\mathcal{L}_f$ is defined by Eq. (27). δy_f can be expressed as

$$\delta y_f = \frac{\delta c_t}{c_0}\eta_1 + B_c e^{-2\pi R_0/c_0\tau_R}\eta_{v,0}, \tag{54}$$

where η_1 is defined in Eq. (32). $\eta_{v,0}$ obeys

$$\mathcal{L}_f(\eta_{v,0}) = [Y_f(x) - Y_b(x)]\left[1 + \left(\frac{dY_f}{dx}\right)^2\right]^{3/2}, \tag{55}$$

with the boundary conditions $\eta_{v,0}(0) = 0, (d\eta_{v,0}/dx)(0) = 2/3$.

In the same way, we obtain, in the tip region, the lowest-order correction δy_b to the back interface of the critical finger $Y_b(x)$,

$$\mathcal{L}_b(\delta y_b)=\frac{\delta c_t}{c_0}\left[1+\left(\frac{dY_b}{dx}\right)^2\right]+\left[\left(B_c\frac{\delta c_t}{c_0}-\delta B - B_c e^{-(2\pi R_0/c_0\tau_R)}\right)[Y_f(x)-Y_b(x)]-B_c\delta y_f\right]\times\left[1+\left(\frac{dY_b}{dx}\right)^2\right]^{3/2}, \tag{56}$$

where the linear operator $\mathcal{L}_b$ is defined by Eq. (28). Equation (56) is similar to Eq. (26) and can be analyzed in the same way. The solvability condition that should be obeyed in order for δy_b not to diverge exponentially as $x\to+\infty$ is found by integrating both members of Eq. (56) with the zero mode $\xi(x)$ of the adjoint of $\mathcal{L}_b$. This gives the following generalization of Eq. (24):

$$K\frac{\delta c_t}{c_0}=\delta B+B_c J\exp\left(-\frac{2\pi R_0}{c_0\tau_R}\right), \tag{57}$$

where $K\simeq 0.630$ [Eq. (37)] and the constant J is

$$J=1+B_c\frac{I_{v,0}}{I_3}\simeq 1.872. \tag{58}$$

I_3 is defined by Eq. (36) and $I_{v,0}$ is given in terms of $\xi(x)$ Eq. (33), and $\eta_{v,0}$, Eq. (55), by

$$I_{v,0}=\int_0^{+\infty}dx\,\xi(x)\,\eta_{v,0}\left[1+\left(\frac{dY_b}{dx}\right)^2\right]^{3/2}=12.553. \tag{59}$$

To complete the analysis, it remains to match the tip region to the outer part of the spiral. As one moves away from the tip, the finger width $Y_f(x)-Y_b(x)$ relaxes exponentially toward its asymptotic value $2/B_c$ on the scale of the tip region. Therefore in the intermediate and far region, $\alpha\delta v_f(r)/c_0$, Eq. (52), is equal to lowest order to $2\exp(-2\pi R_0/c_0\tau_R)$ and the matching equation becomes instead of Eq. (42)

$$\frac{c_t-c_0}{c_0}+2\exp\left(-\frac{2\pi R_0}{c_0\tau_R}\right)+\frac{\epsilon}{c_0R_0}x=\frac{1}{2}\left(\frac{dy}{dx}\right)^2+\frac{d^2y}{dx^2}. \tag{60}$$

Matching with the tip region gives in a similar way

$$2^{-1/3}\left(\frac{c_0R_0}{\epsilon}\right)^{2/3}\left[\frac{c_t-c_0}{c_0}+2\exp\left(-\frac{2\pi R_0}{c_0\tau_R}\right)\right]=a_1\simeq -2.338\ldots. \tag{61}$$

The difference between Eqs. (61) and (38) is simply that c_t is not compared to the velocity of a single planar pulse but to the velocity of a train of pulses of wavelength $2\pi R_0$ (the asymptotic wavelength of the spiral to lowest order). Comparing Eqs. (57) and (61) determines the radius R_0 of a steadily rotating spiral as a function of the medium characteristics B,

$$B_c-B=Kb\left(\frac{\epsilon}{c_0R_0}\right)^{2/3}+(B_cJ+2K)\exp\left(-\frac{2\pi R_0}{c_0\tau_R}\right). \tag{62}$$

The medium disturbance due to the spiral previous passage has two distinct effects which are comparable to lowest order: (1) the medium ''excitability'' is reduced in the tip region, which modifies the tip velocity [Eq. (57)], and (2) the tip velocity should be compared to the velocity of a periodic train of planar waves which is slower than the velocity of a single planar pulse.

V. DERIVATION OF KINEMATIC THEORY

We consider now the spiral dynamics in the vicinity of the line $\Delta_c(\epsilon)$ (for $\epsilon\ll 1$). In this limit, several simplifying features made the previous analysis of the steady states possible. These still hold when one is interested in an unsteady motion taking place on a time scale comparable to the steady rotation period which is long compared to the time scales of the internal modes of the wave tip.

(i) The dominant effect which shapes both the steady spirals and retracting finger tips is the curvature dependence of the normal velocity. As a consequence, the shape of a wave tip is close to a critical finger up to a distance ℓ from the tip where the curvature effects have become small enough to be comparable to the velocity difference between the tip and planar front velocity, namely, when $c_0-c_t\sim\epsilon R_{\rm tip}/\ell^2$ [where we have evaluated the curvature $-d^2Y_f/dx^2\sim R_{\rm tip}/\ell^2$ at $x\sim\ell$ using the asymptotic behavior $Y_f/R_{\rm tip}\sim\ln(x/R_{\rm tip})$ for $x/R_{\rm tip}\gg 1$]. This yields the relation $\ell\sim R_{\rm tip}/\sqrt{1-c_t/c_0}$ that remains also true in the unsteady case. The motion of this ''solid'' shape can be determined from the knowledge of its instantaneous tangential velocity c_t and of its instantaneous rotation rate ω obtained by extending our previous analysis of the steady states.

(ii) The tangential velocity c_t depends on the ''average'' concentration of the controller v in the vicinity of the tip. The precise definition of the average is obtained by using a solvability condition which generalizes Eqs. (35) and (57).

(iii) A tangential velocity c_t smaller than the asymptotic normal velocity c_0 of the wave gives rise to a rotation of the solid tip at a rate ω which can be estimated as in the steady case. As stated above, the wave tip has a solid character (i.e., is close to a critical finger shape) up to a distance $\ell\sim R_{\rm tip}/\sqrt{1-c_t/c_0}$ from the tip. Since kinematics requires that $\omega\ell\sim c_0-c_t$, one obtains for the rotation rate $\omega\sim c_0/R_{\rm tip}(1-c_0/c_t)^{3/2}$. As shown in Appendix B, this relation is established on the time scale $\sim R_{\rm tip}/(c_0-c_t)$ much shorter than the steady rotation period. Therefore, on this latter slow time scale, the slowly varying rotation rate is linked in an adiabatic manner to the slowly varying tangential velocity by the same relation, Eq. (38) or (61), which relates the steady-state frequency to the tip velocity.

We begin our analysis by considering the kinematics of the wave tip motion. We then compute the tangential velocity of the tip as a function of the concentration of the controller v in the medium left by previous passages of the wave. As a result, we obtain an ordinary differential equation with delay which describes the motion of the wave tip. An analysis of this equation at the linear and the weakly nonlinear levels determines the characteristics of the meandering instability near threshold in the weak excitability limit.

A. Parametrization of the wave tip motion

We use polar coordinates (r,θ) with the origin at the center of the circular steady spiral core. The wave tip motion is determined by its tangential velocity $c_t(\{v\})$, a functional of the (space- and time-dependent) controller concentration which will be computed in the next subsection, and by the rotation rate of the shape (or, equivalently, by the radius of curvature of the tip trajectory). We use a complex notation $z(t)=r(t)\exp(i\theta)$ to denote the tip position. Then, the tip velocity is $|\dot{z}|$ and the shape rotation rate $\mathrm{Im}(\ddot{z}\dot{\bar{z}}/|\dot{z}|^2)$ where time differentiation is denoted by a dot and $\bar{z}$ is the complex conjugate of z. The tip motion is thus determined by the two equations

$$|\dot{z}|=c_t(\{v\}), \tag{63}$$

$$\mathrm{Im}(\ddot{z}\dot{\bar{z}}/|\dot{z}|^2)=c_t(\{v\})/R_i[c_t(\{v\})], \tag{64}$$

where at this stage $c_t(\{v\})$ can be thought of as a given function of time. The instantaneous radius of rotation R_i is a function of $c_t(\{v\})$ given to lowest order in the interaction parameter by Eq. (61),

$$\left(\frac{c_0R_i}{\epsilon}\right)^{2/3}\left[\frac{c_t-c_0}{c_0}+2\exp\left(-\frac{2\pi R_0}{c_0\tau_R}\right)\right]=-b. \tag{65}$$

We will actually find that the meander threshold occurs before a significant modification of the steady-state radius by the interaction so that Eq. (65) can be replaced by the simpler Eq. (38),

$$R_i[c_t]\simeq\frac{\epsilon}{c_0}\left(\frac{bc_0}{c_0-c_t}\right)^{3/2}. \tag{66}$$

We consider the motion of a spiral tip which is displaced from its steady-state position $z=[R_0+\epsilon q(t)/c_0]e^{i\omega_1 t+\psi(t)}$ (see Fig. 3). We restrict ourselves to displacements of the tip which are comparable to the tip radius of curvature ϵ/c_0 [i.e., $q(t)\sim 1$] and therefore small compared to the radius of the steady core R_0. As a consequence of the tip displacement, the controller concentration and thus $c_t(\{v\})$ and R_i depart slightly from their steady-state values, $c_t(\{v\})=c_t^0+\delta c_q(\{v\}), R_i=R_0+\delta R_i$.

We assume (and will check *a posteriori*) that the time scale of the unsteady motion is of the order of the steady-state period $T_0=2\pi/\omega_1$. We expand Eqs. (63) and (64) in the small parameter $\epsilon/(c_0R_0)$ and keep only the dominant terms, $|\dot{z}|=\omega_1R_0[1+\dot{\psi}/\omega_1+q\epsilon/(c_0R_0)+\cdots]$, $\mathrm{Im}(\ddot{z}\dot{\bar{z}}/|\dot{z}|^2)=\omega_1[1+\dot{\psi}/\omega_1-\epsilon\ddot{q}/(c_0\omega_1^2R_0)+\cdots]$. Equation (63) gives therefore at lowest order in $\epsilon/(c_0R_0)$

$$\dot{\psi}=\frac{\delta c_q}{R_0}-\frac{\epsilon}{c_0R_0}\omega_1 q, \tag{67}$$

which shows that $\dot{\psi}/\omega_1\sim\epsilon/(c_0R_0)$. Using this scaling, Eq. (64) becomes at lowest order

$$-\frac{\epsilon}{c_0R_0}\frac{\ddot{q}}{\omega_1}+\dot{\psi}=\frac{\delta c_q}{R_0}-c_t^0\frac{\delta R_i}{R_0^2}. \tag{68}$$

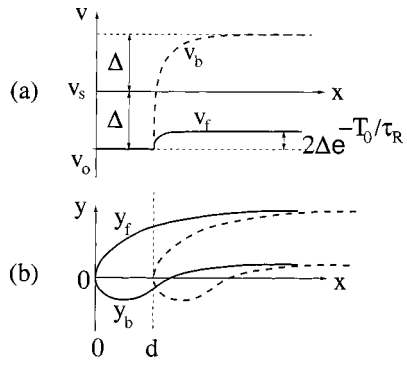

FIG. 7. Schematic plot illustrating (a) the variation of the controller field v on the instantaneous wave front, v_f (solid line), resulting from the previous passage of the spiral wave at the same angular position with the tip displaced radially outwards by d. The dashed line in (a) indicates the variation of v on the wave back, v_b, at the time of the previous passage of the spiral. The solid and dashed line in (b) represent the spiral boundary at the present time (solid line) and at its previous passage (dashed line). Note that the excitability averaged along the instantaneous wave front is higher than for steady-state rotation due to the radial displacement after one rotation. Our formalism provides a rigorous procedure for calculating how the instantaneous tangential velocity of the wave tip changes in response to this spatially varying excitability.

We obtain the equation for the radial motion of the tip by substituting in Eq. (68) the expression (67) of $\dot{\psi}$,

$$\ddot{q}+\omega_1^2q=\omega_1^2\delta R_ic_0/\epsilon. \tag{69}$$

Finally, it is convenient to use the tip angular position $\theta=\omega_1t+\psi(t)$ instead of time. To lowest order in q/R, this simply gives

$$\frac{d^2q}{d\theta^2}+q=\frac{c_0R_i'[c_t^0]}{\epsilon}\delta c_q, \tag{70}$$

with

$$\frac{c_0R_i'[c_t^0]}{\epsilon}=\frac{3}{2bc_0}\left(\frac{c_0R_0}{\epsilon}\right)^{5/3} \tag{71}$$

from a differentiation of Eq. (65). In order to have a closed equation for q, it remains to express δc_q in terms of the previous positions of the wave. We now proceed to this task.

B. Computation of the tangential tip velocity for self-interacting spirals

We consider successive passages of the wave tip by the angular position θ. The successive radial displacements of the tip are $\ldots,\epsilon q(\theta-2\pi)/c_0,\epsilon q(\theta)/c_0,\epsilon q(\theta+2\pi)/c_0,\ldots$. Let us consider the passage at the position $R_0+\epsilon q(\theta)/c_0$ in the Cartesian coordinate system (x,y) attached to the wave tip (see Fig. 7) in which we choose to measure lengths in units of ϵ/c_0. The controller concentration $v_f(x;\theta)$ in the medium just ahead of the front interface is related by the controller recovery kinetics Eq. (8) to the controller concentration left just behind the back interface $v_b(x;\theta-2\pi)$ at the previous passage. At dominant order in

$\epsilon/(c_0 R_0)$, one can neglect the tip width compared to the core perimeter and the time interval between two passages of the spiral by the same angular position can be taken equal to the steady spiral period T_0,

$$v_f(x;\theta) - v_0 = \exp\left(-\frac{T_0}{\tau_R}\right) \times [\, v_b(x+q(\theta)-q(\theta-2\pi);\theta-2\pi) - v_0]. \tag{72}$$

In Eq. (72), note that $v_f(x;\theta)$ is related to $v_b(x+q(\theta)-q(\theta-2\pi);\theta-2\pi)$ since the argument in v_f refers to a frame attached to the wave tip with origin at $R_0+\epsilon q(\theta)/c_0$ whereas the origin of the coordinate for v_b is at $R_0+\epsilon q(\theta-2\pi)/c_0$.

The controller concentrations v_f and v_b at the same passage are also simply related by the controller production equation in the excited region (8),

$$v_b(x;\theta) = v_f(x;\theta) + \epsilon \frac{y_f(x) - y_b(x)}{c_0 c_t \tau_e}. \tag{73}$$

Iterating back in time Eqs. (72) and (73), we see that $v_f(x;\theta)$ depends in principle on the positions of the tip, at all previous passages by the angular position θ. However, the memory of the position $q(\theta - n2\pi)$ is suppressed by the nth power of the small parameter $\exp(-T_0/\tau_R)$. Therefore, to dominant order the controller concentration only depends on the position of the tip at the previous passage,

$$v_f(x;\theta) = v_0 + \epsilon e^{-T_0/\tau_R} \frac{y_f(x+d(\theta)) - y_b(x+d(\theta))}{c_t c_0 \tau_e} \times \Theta(x+d(\theta)), \tag{74}$$

where we have defined the relative displacement of the tip between its two passages $d(\theta) = q(\theta) - q(\theta-2\pi)$. Θ is the usual Heaviside step function, $\Theta(x)=0$ for $x<0$ and $\Theta(x)=1$ otherwise. Equation (74) determines the controller concentration on the front interface at θ as a function of $q(\theta) - q(\theta-2\pi)$. It is now an easy task to generalize the previous computations and obtain the tip tangential velocity corresponding to this concentration.

As for steady interacting spirals, we obtain for the front interface in the tip region

$$\frac{d^2 y_f}{dx^2} = \frac{c_t}{c_0}\left[1+\left(\frac{dy_f}{dx}\right)^2\right] - \left[1 - \frac{\alpha}{c_0}[\, v_f(x;\theta) - v_0]\right] \times \left[1+\left(\frac{dy_f}{dx}\right)^2\right]^{3/2}. \tag{75}$$

The only difference with Eq. (51) is that $\delta v_f = v_f(x;\theta) - v_0$ is now given by Eq. (74). Expanding Eq. (75) around the critical finger shape, $y_f = Y_f + \delta y_f$, one obtains, as before,

$$\mathcal{L}_f(\delta y_f) = \frac{\delta c_t}{c_0}\left[1+\left(\frac{dY_f}{dx}\right)^2\right] + B_c e^{-T_0/\tau_R}[\, Y_f(x+d(\theta)) - Y_b(x+d(\theta))]\Theta(x+d(\theta))\left[1+\left(\frac{dY_f}{dx}\right)^2\right]^{3/2}, \tag{76}$$

with the solution

$$\delta y_f = \frac{\delta c_t}{c_0}\eta_1 + B_c \exp(-T_0/\tau_R)\,\eta_{v,d(\theta)}. \tag{77}$$

The linear operator $\mathcal{L}_f$ is defined by Eq. (27), η_1 is defined in Eq. (32), and $\eta_{v,d}$ is the solution of

$$\mathcal{L}_f(\eta_{v,d}) = [\, Y_f(x+d) - Y_b(x+d)]\Theta(x+d)\left[1+\left(\frac{dY_f}{dx}\right)^2\right]^{3/2}, \tag{78}$$

which generalizes Eq. (55), with the boundary conditions at $x=0$, $\eta_{v,d}(0)=0, \eta_{v,d}(x) \sim \sqrt{x/2}[\, Y_f(d) - Y_b(d)]\Theta(d)$ for $x \ll 1$.

Similarly, the back interface equation in the tip region is

$$\frac{d^2 y_b}{dx^2} = \frac{c_t}{c_0}\left[1+\left(\frac{dy_b}{dx}\right)^2\right] + \left\{1 - \frac{\alpha}{c_0}[\, v_f(x;\theta) - v_0] - \frac{\epsilon\alpha}{c_t c_0^2 \tau_e}[\, y_f(x) - y_b(x)]\right\}\left[1+\left(\frac{dy_b}{dx}\right)^2\right]^{3/2}. \tag{79}$$

After linearization around the back interface of the critical finger, $y_b(x) = Y_b(x) + \delta y_b(x)$, one obtains for the correction δy_b,

$$\mathcal{L}_b(\delta y_b) = \frac{\delta c_t}{c_0}\left[1+\left(\frac{dY_b}{dx}\right)^2\right] + \left\{\left(B_c \frac{\delta c_t}{c_0} - \delta B\right) \times [\, Y_f(x) - Y_b(x)] - B_c e^{-T_0\tau_R}\{Y_f(x+d(\theta)) - Y_b(x+d(\theta))\}\Theta(x+d(\theta)) - B_c \delta y_f\right\} \times \left[1+\left(\frac{dY_b}{dx}\right)^2\right]^{3/2}. \tag{80}$$

Multiplying both sides of Eq. (80) by the zero mode $\xi(x)$ of the adjoint of $\mathcal{L}_b$ and integrating from $x=0$ to $+\infty$ gives

$$\frac{\delta c_t}{c_0}[I_1 + B_c(I_3 - I_2)] = \delta B I_3 + B_c e^{-T_0/\tau_R}[I_{3,d(\theta)} + B_c I_{v,d(\theta)}], \tag{81}$$

where the definite integrals I_1, I_2, I_3 have been defined in Eq. (36) and $I_{3,d}, I_{v,d}$ are given by

$$I_{3,d} = \int_0^{+\infty} dx\, \xi(x)[\, Y_f(x+d) - Y_b(x+d)]\Theta(x+d) \times \left[1+\left(\frac{dY_b}{dx}\right)^2\right]^{3/2},$$

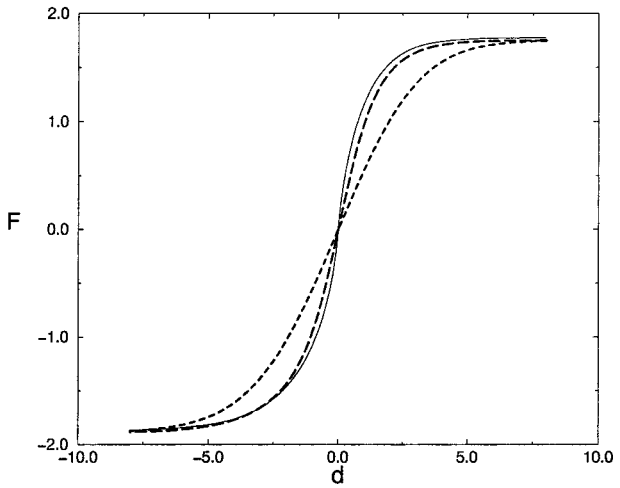

FIG. 8. Graph of the spiral self-interaction function $F(d)$ vs tip displacement d for different controller diffusion lengths: $\ell_D=0$ (solid line), $\ell_D=1$ (long-dashed line), and $\ell_D=3$ (short-dashed line). The generalization of F for finite controller diffusion is considered in Sec. VI A and Appendix C.

$$I_{v,d}=\int_0^{+\infty} dx\,\xi(x)\,\eta_{v,d}\left[1+\left(\frac{dY_b}{dx}\right)^2\right]^{3/2}. \tag{82}$$

Finally, this gives the tangential tip velocity as a function of the tip displacement,

$$\frac{\delta c_t}{c_0}=\frac{\delta B}{K}+\frac{B_c}{K}e^{-T_0/\tau_R}\{J+F(q(\theta)-q(\theta-2\pi))\}, \tag{83}$$

where the constants $K\simeq 0.630$ and $J\simeq 1.872$ are defined in Eq. (37) and Eq. (58). The function $F(d)\equiv[(I_{3,d}+B_cI_{v,d})/I_3-J]$ vanishes at $d=0$ and is plotted in Fig. 8 [44].

Comparing Eq. (83) with Eq. (57) for the steady case shows that the change in tangential velocity due to the tip displacement is

$$\delta c_q=c_0\frac{B_c}{K}e^{-T_0/\tau_R}F(q(\theta)-q(\theta-2\pi)). \tag{84}$$

C. Computation of the tangential velocity in other cases

We conclude this section by emphasizing that, although the present kinematic theory is quite general, the precise expression for the tangential tip velocity that is to be used in conjunction with Eq. (70) depends on the application at hand. For example, Eq. (84) above is valid for self-interacting spirals without external forcing and is therefore perfectly suited to analyze meander in the next section, or interacting multiarmed spirals with a minor modification given in Sec. VIII. For the non-self-interacting spiral with an excitability that varies slowly in space or time (Sec. VII A), one can use directly the results for steady-state rotation [Eq. (24)], whereas under the action of an external field (Sec. VII B) one needs to compute a different expression for the tangential velocity. The general procedure, however, is clear. In each case, the tangential velocity depends on the average controller variable in the tip region and can be computed from a solvability condition.

VI. MEANDER

In this section we analyze the classic meandering instability in a linear and nonlinear regime. Substitution of Eq. (84) in Eq. (70) expresses the right-hand side of Eq. (70) as a function of $q(\theta)-q(\theta-2\pi)$ and provides the differential equation with delay governing the tip motion

$$\frac{d^2q}{d\theta^2}+q=mF(q(\theta)-q(\theta-2\pi)). \tag{85}$$

The parameter m is given by

$$m=\frac{3B_c}{2bK}\left(\frac{R_0c_0}{\epsilon}\right)^{5/3}\exp(-T_0/\tau_R). \tag{86}$$

Values of m of order unity are reached when $(R_0c_0/\epsilon)^{5/3}\exp(-T_0/\tau_R)\sim O(1)$. In this parameter regime, one can use the simple formula (39) to estimate the spiral parameters since in Eq. (62) the correction term (the second term on the right-hand side) is of order $(R_0c_0/\epsilon)^{2/3}\exp(-2\pi R_0/c_0\tau_R)\sim O(1)$ compared to the first term on the right-hand side and therefore smaller by $\epsilon/(R_0c_0)$. This provides the explicit expression of m in terms of the parameter B which characterizes the medium

$$m=\frac{3B_c(bK)^{3/2}}{2(B_c-B)^{5/2}}\exp\left[-\frac{2\pi\epsilon}{c_0^2\tau_R}\left(\frac{bK}{B_c-B}\right)^{3/2}\right]. \tag{87}$$

A. Linear stability analysis and instability criterion

We begin by studying the linear stability of Eq. (85) around $q=0$, that is, the linear stability of steady rotation. For $q\ll 1$, one obtains

$$\frac{d^2q}{d\theta^2}+q=\alpha[q(\theta)-q(\theta-2\pi)], \tag{88}$$

where we have introduced $\alpha=mF'(0)$. Seeking q under the form $q=A\exp(\sigma\theta)$ gives the eigenvalue equation

$$\sigma^2+1=\alpha[1-\exp(-2\pi\sigma)]. \tag{89}$$

For any α, $\sigma_\pm=\pm i$ are isolated solutions of Eq. (89). They simply correspond to the two translation modes of the spiral: for a steady spiral which is slightly displaced from the origin and centered at (x_0,y_0) with $x_0\ll R, y_0\ll R$, the distance of the wave tip to the origin varies sinusoidally as $q=|z_0+R_0\exp(i\theta)|-R_0=x_0\cos\theta+y_0\sin\theta$.

The other solutions of Eq. (89) vary with α. For small $\alpha>0$, the right-hand side of Eq. (89) is comparable to its left-hand side only if the real part of σ is large and negative, that is, $\mathrm{Re}(\sigma)\sim -1/2\pi\ln(\alpha)$. Therefore, for small α, all eigenvalues (different from the two translation modes) have a negative real part and the steady rotation is stable. As α is increased, the eigenvalues move continuously in the complex plane. An instability occurs when the real part of some of

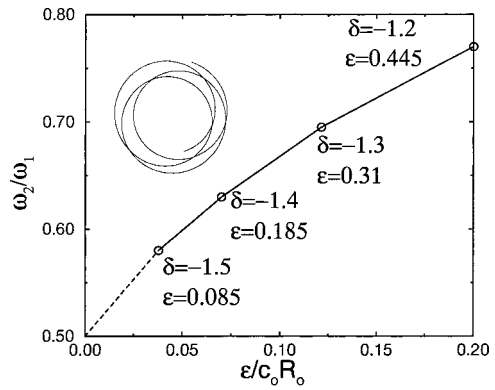

FIG. 9. Plot of ω_2/ω_1 vs $c_0/\epsilon R_0$ obtained by simulations of FitzHugh-Nagumo kinetics with $f(u,v)=3u-u^3-v$ and $g(u,v)=u-\delta$ (solid line and circles). $c_0=(\delta^3-3\delta)/2^{1/2}$. The dashed line represents the extrapolation to the asymptotic limit $\omega_2/\omega_1=1/2$ predicted by our analysis. These simulations were carried out using a second-order accurate direction implicit scheme with $dx/\epsilon=0.33$ and $dt/\epsilon=0.1$. The inset shows an example of a large core meander pattern for $\epsilon=0.180$ and $\delta=-1.4$, where $\omega_2/\omega_1\simeq 0.67$.

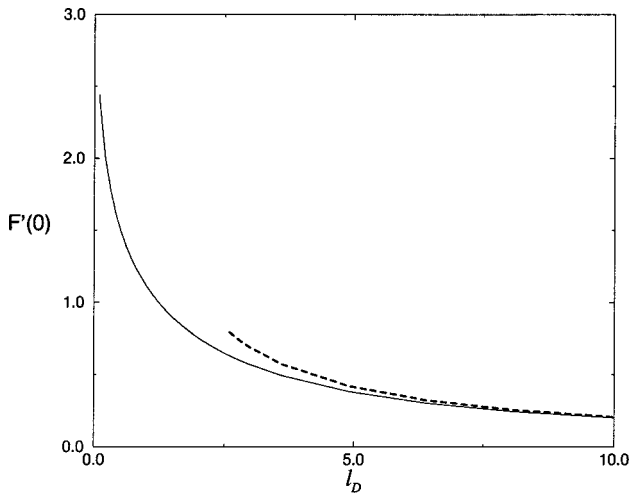

FIG. 10. Derivative at $d=0$ of the spiral self-interaction function $F(d;\ell_D)$ vs the diffusion length ℓ_D. The dashed line shows the large-ℓ_D [Eq. (C26)] asymptotic behavior.

them traverses zero and becomes positive. This happens at the critical value $\alpha=\alpha_c$ where Eq. (89) has a purely imaginary root $\sigma=i\Omega$, namely, for

$$\alpha_c[1-\cos(2\pi\Omega)]=1-\Omega^2, \tag{90}$$

$$\alpha_c\sin(2\pi\Omega)=0, \tag{91}$$

Eq. (91) requires that Ω be a half integer. Equation (90) can therefore be rewritten as $1-\Omega^2=\alpha_c[1-(-1)^{2\Omega}]$, the only solution of which is, for $\alpha_c>0$, $\Omega=\pm 1/2, \alpha_c=3/8$.

We therefore conclude that for $0<\alpha<\alpha_c$ all eigenvalues different from $\sigma_\pm$ have a negative real part. As α increases past $\alpha_c=3/8$, a couple of eigenvalues traverse the imaginary axis and acquire a positive real part. The value $\alpha=\alpha_c$ is thus the threshold of a Hopf bifurcation and corresponds to the meander onset with a frequency ratio at threshold $\omega_2/\omega_1=1/2$. This ratio is consistent with the extrapolation to infinite core radius of numerical simulation results as shown in Fig. 9.

It is interesting to note that as α is further increased, the frequency of the two linearly unstable modes decreases and the two unstable eigenvalues become purely real for $\alpha>\alpha_r$ (α_r is simply determined as the value of α for which Eq. (89) has a doubly degenerate root, $\alpha_R=(\sigma_r/\pi)\exp(2\pi\sigma_r)$ with $\sigma_r^2+1=(\sigma_r/\pi)[\exp(2\pi\sigma_r)-1]$ which gives $\sigma_r\simeq 0.375$ and $\alpha_r\simeq 1.260$). This may explain why a previous analysis performed at small ϵ, but away from ∂M [29], yielded only real unstable modes instead of complex conjugate eigenvalues as expected from a Hopf bifurcation.

Given the expression (87) of the constant m, the criterion for meander onset $\alpha_c=mF'(0)=1/2$ implies that, for small ϵ, the meander boundary $\Delta_m(\epsilon)$ lies close in the (ϵ,Δ) plane to the critical finger boundary $\Delta_c(\epsilon)$ (see Fig. 1) with $\Delta_c-\Delta_m\sim\epsilon^{5/9}/\ln^{2/3}[\epsilon^{5/9}/F'(0)]$.

In the pure sharp boundary description with no diffusion of the controller v field, the behavior of the function F is nonanalytic at short distance $F(d)\sim -0.576d\ln(|d|)$ for $d\ll 1$ as shown in Appendix C. This implies that, in this context, the onset of meander occurs right at the critical finger boundary. However, when one starts from the full reaction-diffusion equation (3), (4), the interface has a finite width of the order of ϵ. This eliminates any short distance nonanalyticity and cutoff the divergence of $F'(d)$ at $d\sim\Delta\sim\epsilon^{1/3}$. This gives the estimate $F'(0)\sim-\ln(\epsilon)$ and $\Delta_c-\Delta_m\sim\epsilon^{5/9}/|\ln(\epsilon)|^{2/3}$.

The nonanalyticity of F also disappears if the slow field v diffuses, that is, if instead of Eq. (6) one has

$$\partial_t v=\gamma\epsilon\nabla^2 v+g(u^\pm(v),v) \quad \text{in} \quad \mathcal{D}^\pm. \tag{92}$$

For a sufficiently small diffusion constant γ, one can neglect entirely the diffusion in the excited region $\mathcal{D}^+$ and consider only a radial diffusion of v in $\mathcal{D}^-$. The controller concentration on the front spiral interface in the tip region is then a smoothened version of Eq. (74),

$$v_f-v_0=\frac{\epsilon e^{-T_0/\tau_R}}{c_0 c_t\tau_E}\int_0^{+\infty}\frac{dx'}{\sqrt{\pi}\ell_D}e^{-[x+d(\theta)-x']^2/\ell_D^2}\times[Y_f(x')-Y_b(x')], \tag{93}$$

$$v_b=v_f+\epsilon(Y_f(x)-Y_b(x))/(c_0 c_t\tau_E). \tag{94}$$

The finite diffusion length $\ell_D=\sqrt{4\epsilon\gamma T_0}c_0/\epsilon$ removes the short distance analyticity and gives a finite first derivative to F at the origin which decreases with increasing ℓ_D as plotted in Fig. 10 (see also Appendix C). This decrease of stability with a decrease of ℓ_D qualitatively agrees with the numerical results of [45]. Of course, diffusion controls the stability only if ℓ_D is much larger than the interface width (or the width of the tip boundary layer). When it is much smaller, stability is controlled by finite interface width effects as discussed above. When the two effects have comparable magnitude, the numerical results of [45] suggest that more complex stability diagrams are possible (i.e., there is a region of reentrant stability). It would be interesting to see if this could be explained by a more complete computation of F taking into account both finite interface effect and diffusion of v.

We conclude this subsection with a simple interpretation of the obtained results. The existence and magnitude of the instability threshold can be understood by considering a displacement of the wave tip by a small distance d towards the outside of its steady circular trajectory. Since the outside of the core is slightly less excitable than the inside, this outward displacement will cause the spiral tip to propagate in a less excitable medium and to rotate on a new larger radius $R_i = R_0 + \delta R_i > R_0$. The fact that $\delta R_i > 0$ by itself is not sufficient to create an instability. It is only if δR_i is larger than $\sim d$ that the displacement of the wave tip can be amplified and meander can appear. The excitability change due to the displacement d is $|\delta B| \sim d/R_{\rm tip} e^{-T_0/\tau_R}$ where the exponential factor simply reflects the global attenuation of excitability variations between two passages of the wave. This excitability change leads to a variation of the rotation radius $\delta R_i \sim dR_0/dB\,\delta B$. Thus, $\delta R_i/d \sim (dR_0/dB)/R_{\rm tip} e^{-T_0/\tau_R} \sim m$ and the onset of meander occurs for m of order unity in agreement with the above stability analysis. The period doubling like character of the unstable motion (i.e., $\omega_2/\omega_1 = 1/2$) can also be attributed to the radial gradient of excitability at the edge of the spiral core. A wave tip displaced outward from the center at a given passage will propagate, at its next passage, in a medium more excitable than the one produced by steady rotation. This will cause the tip to execute this second turn on a smaller radius and thus, to propagate again in a less excitable medium and with a larger radius at the next cycle, leading to the period doubling behavior. As we shall discuss in Sec. IX, this picture is modified by finite core effects that roughly make trajectories of larger radius take a longer time to complete one rotation. This effect causes the spiral tip to return sooner inside the core and, in turn, leads ω_2/ω_1 to increase away from 1/2 with decreasing R_0.

B. Nonlinear dynamics

We now carry out a standard weakly nonlinear analysis of the wave tip equation of motion (85) and show that the bifurcation to meander is supercritical in agreement with existing numerical studies of reaction-diffusion models [14,15]. This analysis also allows us to characterize more precisely the epicyclelike trajectories of the wave tip in the large core limit. Next, we integrate Eq. (85) numerically and explore the nonlinear regime further away from the bifurcation point.

1. Weakly nonlinear analysis

To carry out the weakly nonlinear analysis, we first expand the function F on the right-hand side of Eq. (85) up to cubic terms, which yields the equation

$$\frac{d^2q}{d\theta^2} + q = \alpha \Delta q + \Gamma (\Delta q)^2 - \beta (\Delta q)^3, \tag{95}$$

where we have defined

$$\Delta q \equiv q(\theta) - q(\theta - 2\pi) \tag{96}$$

and the constants

$$\alpha = mF'(0), \tag{97}$$

$$\Gamma = mF''(0)/2, \tag{98}$$

$$\beta = -mF'''(0)/6. \tag{99}$$

In writing Eq. (95), we have supposed that the nonanalyticity of F in the pure sharp boundary limit has been taken care of either by taking into account finite interface width effects or by a small diffusion of ν [e.g., for $\ell_D = 1$ one has $F'(0) \simeq 1.12, F''(0) = 2.810^{-2}, F'''(0) \simeq -1.1$]. Note, however, that Eq. (85) is well defined even for the nonanalytic sharp boundary F. We shall comment in the next subsection on the small amplitude behavior in this case. Equation (95) is valid in a regime where the parameter

$$\mu \equiv \alpha - \alpha_c, \tag{100}$$

which defines the distance above the onset ($\alpha_c = 3/8$) of the meandering instability, is small. Next, we seek perturbatively for time periodic solutions of Eq. (95) of the form

$$q(\theta) = q_0 + \sum_{n=1}^{\infty} A_n e^{in\Omega\theta} + \text{c.c.}, \tag{101}$$

where as before $\Omega = \omega_2/\omega_1$ is the ratio of the Hopf frequency at the meander bifurcation and the primary angular rotation frequency. Substituting Eq. (101) into Eq. (95) and focusing on the first two modes ($n=1$ and $n=2$), we obtain at once that

$$(-\Omega^2 + 1) A_1 = \alpha(1-\zeta) A_1 + 2\Gamma A_2 \bar{A}_1 (1-\bar{\zeta})(1-\zeta^2) - 3\beta (1-\zeta)^2 (1-\bar{\zeta}) A_1 |A_1|^2, \tag{102}$$

$$(-4\Omega^2 + 1) A_2 = \Gamma (1-\zeta)^2 A_1^2 + \alpha (1-\zeta^2) A_2 - 2\beta (1-\zeta) \times (1-\bar{\zeta})(1-\zeta^2) A_2 |A_1|^2, \tag{103}$$

where we have defined

$$\zeta = e^{-i2\pi\Omega} \tag{104}$$

and $\bar{\zeta}$, $\bar{A}_n$ denote the complex conjugates of ζ, A_n, respectively. Eliminating A_2 between the above two relations, and neglecting the terms proportional to $(1-\zeta)^2(1-\bar{\zeta}) A_2 |A_1|^2$ on the right-hand side of Eq. (102) (which can be checked to be of higher order at the end), we obtain that

$$\Omega^2 - 1 + \alpha(1-\zeta) + \left[2\Gamma^2 \frac{(1-\bar{\zeta})(1-\zeta)^2(1-\zeta^2)}{1 - 4\Omega^2 - \alpha(1-\zeta^2)} - 3\beta (1-\zeta)^2 (1-\bar{\zeta}) \right] |A_1|^2 = 0. \tag{105}$$

The condition that the real and imaginary parts of the left-hand side of the above equation must vanish independently provides two independent relations that determine Ω and A_1. Next, expanding Eq. (105) to first order in the frequency shift $\Omega - 1/2$, we obtain

$$-3/4+2\alpha+(1-i2\pi\alpha_c)(\Omega-1/2)$$
$$-\left[24\beta+\frac{16i\Gamma^2\pi}{1+i\alpha_c\pi}\right]|A_1|^2=0. \tag{106}$$

The conditions that the real and imaginary parts of the above equation must vanish lead after simple algebraic manipulations to the relations

$$|A_1|=\sqrt{c_1\mu}, \tag{107}$$

$$\Omega-1/2=-c_2\mu, \tag{108}$$

where c_1 and c_2 are constants defined by

$$1/c_1=12\beta+\frac{\Gamma^2}{3}\frac{9\pi^2+32}{1+(3\pi/8)^2}, \tag{109}$$

$$c_2=\frac{64c_1\Gamma^2}{3[1+(3\pi/8)^2]}. \tag{110}$$

Equation (103) implies that at leading order in μ,

$$A_2=\frac{\Gamma A_1^2}{(1/2-\Omega)(1+i3\pi/8)} \tag{111}$$

or, using Eqs. (107) and (108),

$$|A_2|=\frac{3}{64\Gamma}\sqrt{1+(3\pi/8)^2}. \tag{112}$$

In addition, substituting Eq. (101) into Eq. (95), one obtains for $n=0$ that $q_0=8\Gamma|A_1|^2=8\Gamma c_1\mu$. It is simple to work out that higher-order terms in the present expansion must scale as $A_n\sim\mu^{n/2}$ for n odd and $A_n\sim\mu^{n-2}$ for n even. Note that the expansion of Eq. (85) leading to Eq. (95) remains justified because $\Delta q(\theta)$ vanishes as $\mu\to0$ even though A_2 remains of order unity (i.e., $A_2\{\exp[i2\Omega\theta]-\exp[i2\Omega(\theta-2\pi)]\}\sim c_2\mu$ in this limit).

Let us now examine the meander trajectory of the wave tip. For this purpose it is convenient to define the dimensionless coordinate $Z=X+iY=Re^{i\theta}/R_{\rm tip}$, which is scaled by the tip radius $R_{\rm tip}=\epsilon/c_0$, and is given by

$$Z=X+iY=(\rho_0+q)e^{i(\theta+\psi)}, \tag{113}$$

$$d\psi/d\theta=-(q-q_0)/\rho_0, \tag{114}$$

where we have defined the scaled steady-state radius $\rho_0=R_0R_{\rm tip}$. We have subtracted the θ-independent part of $q(\theta)$ which gives a shift of ω_1 of $O(q_0/\rho_0)$ [Eq. (67)]. Since $1/\rho_0\ll1$, we can expand the above relations to first order in ψ, which yields

$$X+iY=\left(\rho_0+q-i\int(q-q_0)d\theta\right)e^{i(1-q_0/\rho_0)\theta+i\psi_0}. \tag{115}$$

Since the phase factor ψ_0 corresponds to a translation of the center of rotation, we can set $\psi_0=0$, which yields the relation

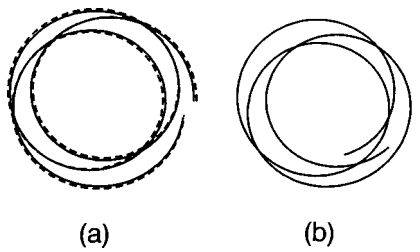

FIG. 11. Comparison of large core meander trajectories obtained (a) by plotting a two-radius epicycle (solid line) with $\Omega=0.735$ and $\rho_1/\rho_0=1/5$ and the predicted three-radius epicycle (dashed line) with $\Omega=0.735$, $\rho_1/\rho_0=1/5$, and $\rho_2/\rho_1=(1-\Omega)/(1+\Omega)$, and (b) by simulation of the FN model with $\epsilon=0.18$ and $\delta=-1.4$. The value of Ω and the ratio ρ_1/ρ_0 used as input in (a) were extracted from the simulation in (b). The total time in (a) and (b) is about $3T_0$.

$$X+iY=\rho_0e^{i\theta}+\sum_{n=1}^{\infty}\left[\bar{A}_n\left(1+\frac{1}{n\Omega}\right)e^{i(1-n\Omega)\theta}+A_n\times\left(1-\frac{1}{n\Omega}\right)e^{i(1+n\Omega)\theta}\right], \tag{116}$$

where the amplitudes A_n dictate the meandering motion of the tip.

Note that in deriving Eq. (116) we have only assumed that q/ρ_0 is small, such that this equation is not restricted to the asymptotic large core limit where $\Omega=1/2$ at the bifurcation. In fact, in the weakly excitable limit that is typically accessible in simulation, Ω is larger than 1/2 at the bifurcation point due to finite core radius corrections $\sim1/\rho_0$ that modify Eq. (85) as discussed in Sec. IX [see, e.g., Eq. (165)]. In this case, the bifurcation is not resonant (i.e., $2\omega_2\neq\omega_1$), and $A_2\sim\mu$ near onset. Equation (116) implies that in this generic case, relevant for usual simulations and experiments, the motion of the tip can be described by keeping only the terms proportional to A_1 and $\bar{A}_1$ in Eq. (116) that is a three-radius epicycle (or epiepicycle)

$$X+iY=\rho_0e^{i\theta}+\rho_1e^{i(1-\Omega)\theta-i\theta_1}-\rho_2e^{i(1+\Omega)\theta+i\theta_1}\qquad(\Omega>1/2), \tag{117}$$

where θ_1 is an arbitrary phase, $\rho_1\sim\sqrt{\mu}$, and

$$\rho_2/\rho_1=(1-\Omega)/(1+\Omega). \tag{118}$$

The fact that ρ_2/ρ_1 vanishes as $\Omega\to1$ may provide an explanation for why the meander trajectories in simulations of reaction-diffusion models of excitable media have been traditionally well fitted by a simple epicycle [Eq. (117) with $\rho_2=0$]. In Ref. [15], it was argued that meander trajectories should generally be epiepicycles close to the onset of instability. It was left unexplained, however, why the ratio ρ_2/ρ_1 turns out to be very small. For the simulation of the FN of Ref. [15], $\Omega\approx0.782$, in which case Eq. (118) predicts that $\rho_2/\rho_1\approx0.12$. This ratio is roughly consistent with the ratio of the amplitudes of the peaks of $1+\Omega$ and $1-\Omega$ in the power spectrum of $X(t)$ in Fig. 4 of [15]. Here, Fig. 11 illustrates that two-radius and three-radius epicycle trajecto-

ries are very close even when Ω departs significantly from unity. Such a small difference is probably hard to resolve experimentally.

Let us now examine the meander trajectory predicted by Eq. (116) in the asymptotic limit where $\Omega = 1/2$, which is more difficult to reach in simulation and experiment. The main difference in this case is that A_2 is $O(1)$ because the bifurcation is resonant, i.e., $A_1^2 e^{i2\Omega\theta}$ act as a periodic drive of the wave tip at the primary frequency $\Omega = 1$. Inserting the results of the weakly nonlinear analysis, Eqs. (107)–(112), into Eq. (116), we obtain that

$$X + iY = \rho_0 e^{i\theta} + \rho_1 e^{i\theta/2 - i\theta_1} - \rho_2 e^{i3\theta/2 + i\theta_1} + \rho_3 e^{i\Omega^*\theta + i(-2\theta_1 + \tan^{-1} 3\pi/8)} \quad (\Omega = 1/2), \tag{119}$$

where we have defined $\Omega^* \equiv 1 - 2\Omega = 2c_2\mu$, θ_1 is an arbitrary phase, and

$$\rho_1 = 3\sqrt{c_1\mu}, \quad \rho_2 = \rho_1/3, \quad \rho_3 = 3\sqrt{1 + (3\pi/8)^2}/(32\Gamma). \tag{120}$$

Consequently, the effect of the resonance when $\Omega = 1/2$ is to add a slow component of motion with frequency $\Omega^* \sim \mu$ around a circle of radius ρ_3 of $O(1)$. Steady-state rotation is approached smoothly when $\mu \to 0$, even though ρ_3 remains finite, because Ω^* vanishes in this limit. Finally, we note that ρ_3 diverges as $1/\Gamma$ in the limit $\Gamma \to 0$. The tangential velocity of the tip around the circle of radius ρ_3, however, scales as $\Omega^* \rho_3 \sim \Gamma$ and vanishes in this limit, which is therefore well behaved.

2. Numerical integration of the wave tip equation

Equation (85) was integrated numerically using the algorithm described in Appendix A. We used both the function F plotted in Fig. 8, and the simple analytical form

$$F(x) = \tanh(x - a) + \tanh(a). \tag{121}$$

This form has qualitatively the same shape as the calculated function F, which is plotted for different ℓ_D in Fig. 8, and yields a qualitatively similar nonlinear behavior. For this reason, all the results presented here are for this simplified form of F defined by Eq. (121) for the choice of parameter $a = 0.2$. As noted earlier, the calculated function F is nonanalytic at the origin in the singly diffusive sharp boundary model and behaves as $-0.576q \ln(|q|)$. When this is used in Eq. (85) for the tip motion, as noted previously, a steady rotation is unstable for all m [Eq. (87)] however small since the slope of F at the origin diverges. The growth of the modulation as one moves away from threshold is, however, much slower than in the analytic case, the amplitude of the modulation being of order $\exp(-cst/m)$. It is interesting to note that requiring this amplitude to be larger than the interface width ϵ, as a criterion for meander threshold in a real small-ϵ model, gives $m \sim cst/|\ln(\epsilon)|$ quite similarly to what was obtained previously by cutting off the slope of F at the scale of the interface width. Away from onset, however, this nonanalyticity does not modify the nonlinear behavior much. For this reason, we shall not treat this case separately.

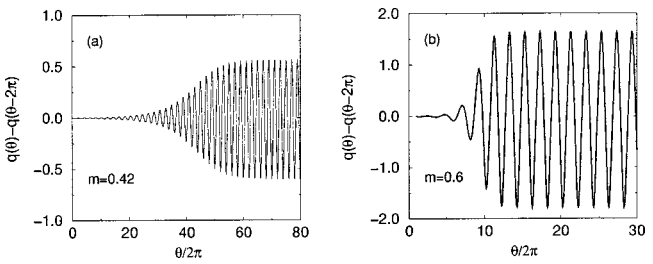

FIG. 12. Plot of $q(\theta) - q(\theta - 2\pi)$ vs $\theta/2\pi$ obtained by numerical integration of the wave tip equation with F defined by Eq. (121) and $a = 0.2$; (a) $m = 0.42$, and (b) $m = 0.6$. The onset of meander for this function F corresponds to $m_c = 0.3902$.

The results of the numerical integration of Eq. (85) are illustrated in Figs. 12 and 13. We have found it convenient to plot $q(\theta) - q(\theta - 2\pi)$, instead of $q(\theta)$ because the latter quantity contains a component $\sim e^{i\theta}$ that only yields a translation of the center of rotation. We have checked that the amplitude of oscillation and the frequency shift of Ω from 1/2 increase quantitatively for small μ as predicted by the weakly nonlinear analysis. Figure 13 shows that the oscillations become more nonlinear with increasing distance from the bifurcation point, but remain periodic with a frequency close to 1/2. The fact that the frequency is rather insensitive to m can be understood by remarking that F [calculated or approximated by Eq. (121) with a small] is close to being an odd function of its argument. For F exactly odd [$\Gamma = mF''(0) = 0$], the weakly nonlinear analysis of the preceding section predicts that $A_n = 0$ for all n even and that there is no nonlinear frequency shift, i.e., $\Omega = 1/2$ for any value of $\mu > 0$. One would therefore naturally expect to find that Ω remains close to 1/2, even far from onset, when F deviates slightly from an odd function.

Finally, it is worth noting that hypermeander (i.e., chaotic meander) is not contained in the large core limit. This is consistent with the fact that hypermeander has been observed numerically in the opposite parameter range of high excitability [12]. In this range, the shape of the spiral boundary is not constant in time on the scale of R_{tip}. It therefore seems likely that the dynamics on this scale plays an important role in hypermeander.

VII. SPIRAL MOTION UNDER EXTERNAL ACTION

Motion of spiral waves can be induced by modulating the medium excitability in space or time or by adding an external field. It is not difficult to extend the approach of Sec. V to describe these effects simply and quantitatively in the large core limit.

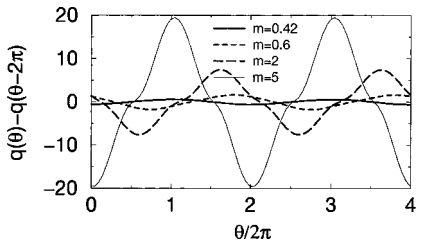

FIG. 13. Plot showing saturated oscillations of $q(\theta) - q(\theta - 2\pi)$ vs $\theta/2\pi$ for different m.

A. Variation of the medium excitability

We consider first the effect of spatial and temporal modulations of the excitability (obtained by changing Δ and/or ϵ into space and/or time). Such a modulation will generally produce a variation of both the planar front velocity c_0 and a variation $\delta B(z,t)$ of the parameter B characterizing the medium. We assume that this variation is small enough to be treated as a perturbation, that $\delta B(z,t)$ varies slowly in time (i.e., on the scale of the spiral rotation period) and in space (i.e., on the scale of the spiral core), and that B is close enough to B_c (i.e., ∂R) so that the spiral self-interaction can be neglected. The radius of curvature of the tip trajectory will then depart from its unperturbed value R_0, $R_i = R_0 + \delta R_i$ with

$$\frac{\delta R_i}{R_0} = \frac{3}{2}\frac{\delta B}{B_c - B} \tag{122}$$

and the variation of c_0 gives a subdominant contribution for B close to B_c. Substituting the above expression into Eq. (69), we obtain at once

$$\ddot{q} + \omega_1^2 q = \frac{3}{2}\frac{c_0 R_0}{\epsilon}\frac{\omega_1^2 \delta B(z,t)}{B_c - B}. \tag{123}$$

Integration of Eq. (123) gives the spiral tip motion resulting from a given space time variation of excitability. As a simple illustration, we show that a global periodic variation of excitability at the spiral frequency induces a spiral drift [19]. When $\delta B = A\cos(\omega_1 t + \phi)$, the right-hand side of Eq. (123) is resonant with the natural oscillation modes of the left-hand side, the translation modes, and induces their growth,

$$q(t) = \frac{3}{4}\frac{c_0 R_0}{\epsilon}\frac{\omega_1 t}{B_c - B} A\sin(\omega_1 t + \phi). \tag{124}$$

A simple way to understand the motion described by Eq. (124) is to remember that for a steady spiral centered close to the origin (compared to the radius of its core), at $z_0 = x_0 + iy_0$, the distance of the wave tip to the origin varies periodically as

$$|R_0 \exp(i\omega_1 t) + z_0| \simeq R_0 + x_0\cos(\omega_1 t) + y_0\sin(\omega_1 t). \tag{125}$$

Comparing the two expressions shows that Eq. (124) describes a linear drift of the spiral,

$$z_0 = \frac{3}{4}\frac{c_0 R_0}{\epsilon}\frac{A}{B_c - B}\omega_1 t[-i\exp(-i\phi)]. \tag{126}$$

The drift direction depends on the relative phase between the spiral rotation and the periodic modulation of excitability: the spiral drifts perpendicularly to the direction $[\exp(-i\phi)]$ of the spiral tip at the maximum excitability viewed from the spiral center. One can note that our derivation of Eq. (126) is simple, but, of course, it breaks down when the spiral center is no longer close to the origin and the linearization giving Eq. (69) and thus Eq. (123) becomes illegitimate. The remedy is standard: a nicer looking derivation is obtained by introducing at the very start of the derivation of Eq. (69) the spiral center z_0 and parametrizing the wave tip as $z = z_0 + [R_0 + \epsilon q(t)/c_0]e^{i\omega_1 t + \psi(t)}$. The slow variation of z_0 with time is obtained by requiring that it cancels the secular term on the right-hand side of Eq. (123).

A time-independent excitability which varies slowly in space is another simple case. The parameter $B(z)$ in Eq. (123) should be evaluated at the spiral tip position. As the spiral tip turns around the spiral core, B varies harmonically in time at the spiral rotation period and the spiral drifts. Since the direction of maximum excitability viewed from the spiral center is along the gradient of B, one concludes that the spiral drifts perpendicularly to the gradient of B, along an isoexcitability line.

B. Drift in an external field and filament tension

It has been reported in previous experimental [20,21,23] and theoretical studies [24,25] that a spiral drifts when it is submitted to a constant external field. Interestingly, the spiral was found to drift at a nonzero angle with the applied external field. In the presence of an external field $\mathbf{E}$ which couples to the activator u, the activator reaction-diffusion (3) becomes

$$\partial_t u = \epsilon\nabla^2 u + f(u,v)/\epsilon - \mathbf{E}\cdot\boldsymbol{\nabla} u. \tag{127}$$

A simple way to determine the effect of $\mathbf{E}$ is to view the wave dynamics in a frame M which moves at velocity $\mathbf{E}$. In such a frame, the supplementary gradient term in Eq. (127) disappears and u simply obeys the fieldless Eq. (3). However, the controller equation is modified. It reads, in the excited region,

$$\partial_t v = 1/\tau_e + \mathbf{E}\cdot\boldsymbol{\nabla} v. \tag{128}$$

The gradient term in Eq. (128) modifies the relation between the tangential tip velocity and the medium parameters. As shown below, one obtains instead of Eq. (37)

$$c_t = c_0 + c_0\frac{B - B_c}{K} + \gamma_\parallel E_\parallel + \gamma_\perp E_\perp, \tag{129}$$

where $E_\parallel$ and $E_\perp$ are the external field component, respectively, parallel and orthogonal to the tangential tip velocity (measured in the frame M). Our sign convention is that $E_\perp > 0$ when it points toward the excited region of the spiral tip. The numerical coefficients $\gamma_\parallel$ and $\gamma_\perp$ are determined below from a solvability condition, as we have now done several times. Before detailing this computation, we show that the spiral drift is a simple consequence of Eq. (129). As above, the wave tip motion is determined by Eqs. (63), (64) where now $z = x + iy$ denotes the position of the wave tip in the frame M and c_t is given by Eq. (129) and depends on the angle between the instantaneous velocity (in the frame M) and the external field $\mathbf{E}$. The form of the function $R_i[c_t]$ is a consequence of the front interface dynamics determined by Eq. (3) which applies in the frame M. Therefore, it still has the large core asymptotic form (66). Writing $c_t = c_t^0 + \delta c_E$ in Eq. (129) as a constant part c_t^0 independent of the external field and a small external field-dependent part $\delta c_E = \gamma_\parallel E_\parallel + \gamma_\perp E_\perp$, we can again copy the analysis of Sec. V A and

simply replace δc_q by δc_E. For a perturbed wave tip circle motion $z=[R_0+\epsilon q(t)/c_0]e^{i\omega_1 t+\psi(t)}$, this gives instead of Eq. (69)

$$\ddot{q}+\omega_1^2 q=\omega_1^2\delta c_E\frac{c_0R_i'[c_t^0]}{\epsilon}=\omega_1^2\frac{3}{2}\frac{c_0R_0}{\epsilon}\frac{\delta c_E}{c_0-c_t^0}. \tag{130}$$

For definiteness, we suppose that the field **E** is parallel to the x axis which gives, to lowest order in the perturbation, $E_\parallel=-E\sin(\omega_1 t)$ and $E_\perp=E\cos(\omega_1 t)$. So, Eq. (130) is again found to be the equation of a harmonic oscillator forced at its natural frequency and the amplitude q of the oscillation diverges in time,

$$\frac{\epsilon}{c_0R_0}q(t)=\frac{3}{4}\frac{E}{c_0-c_t}\omega_1 t[\gamma_\parallel\cos(\omega_1 t)+\gamma_\perp\sin(\omega_1 t)]. \tag{131}$$

Comparing Eq. (131) with the expression of q for a translated spiral (125), one concludes that Eq. (131) describes a spiral drifting away from the origin at constant velocity with

$$x_0=\frac{3}{4}\frac{E}{c_0-c_t}\gamma_\parallel R_0\omega_1 t,$$

$$y_0=\frac{3}{4}\frac{E}{c_0-c_t}\gamma_\perp R_0\omega_1 t. \tag{132}$$

The spiral drift angle θ_D with the external field is therefore

$$\tan(\theta_D)=\gamma_\perp/\gamma_\parallel. \tag{133}$$

Several remarks can be made:

(i) Formally, θ_D is the angle between the drift velocity and the external field in the M frame. However, the drift velocity in the large core limit is dominantly produced by the time-dependent variation of the spiral radius and is much larger than the velocity difference between the laboratory frame and the M frame. Terms of the same order as the velocity difference between the two frames have been neglected in obtaining Eq. (131). It therefore makes no sense to correct θ_D for this velocity difference.

(ii) A constant field produces a spiral drift because the right-hand side of the components of the external field in the tip frame, $E_\parallel=-E\sin(\omega_1 t)$ and $E_\perp=E\cos(\omega_1 t)$, oscillate at the resonant frequency ω_1. A sinusoidal external field oscillating at ω_e has components in the tip frame at $\omega_e+\omega_1$ and $\omega_e-\omega_1$. A spiral drift is therefore induced by an external field when it oscillates at *twice* the spiral frequency ($\omega_e=2\omega_1$), as noted in previous studies [22].

(iii) As stated previously, the derivation of Eq. (132) breaks down when the spiral center is no longer close to the origin and the linearization giving Eq. (131) becomes illegitimate. This can be cured as stated above, by introducing from the start the spiral center the motion of which is determined through the requirement that no secular terms appear on the right-hand side of Eq. (130).

It remains to obtain Eq. (129) and compute the parameters $\gamma_\parallel$ and $\gamma_\perp$. We consider the spiral (in the M frame) in a Cartesian coordinate system attached to the wave tip as in Fig. 3. As before, the front interface $y_f(x)$ simply obeys Eq. (18) in the tip region. However, the controller concentration on the back interface is changed by the external field [Eq. (128)] and this modifies the back equation (19).

We begin by computing the controller concentration on the back interface. The time dependence of the field components can be neglected since it is on the scale of the rotation period, R_0/c_0, which is much longer in the large core limit than the time scale of interest, the spiral width traversal time ϵ/c_0^2. Equation (128) thus shows that in the excited region v obeys

$$v(t,x-E_\perp t,y-E_\parallel t)=v(0,x,y)+t/\tau_e. \tag{134}$$

The concentration $v_b(x)$ on the back interface at the point $(x,y_b(x))$ is related to the controller concentration v_0 on the front interface at the point $(x_f,y_f(x_f)+c_t t(x))$ at a previous time $t(x)$ with

$$x_f=x-E_\perp t(x),$$

$$y_f(x_f)+c_t t(x)=y_b(x)-E_\parallel. \tag{135}$$

x_f and $t(x)$ are functions of x, the considered point of the back interface which can be determined perturbatively for small external field. Writing $x_f=x+\delta x, t(x)=t_0(x)+\delta t(x)$, one obtains $t_0(x)=[y_b(x)-y_f(x)]/c_t, \delta x=-E_\perp t_0(x)$, and $\delta t(x)=t_0(x)(-E_\parallel+E_\perp dy_f/dx|_x)/c_t$. Therefore the controller concentration at abscissa x on the back interface is equal to

$$\begin{aligned} v_b(x)&=v_0-t(x)/\tau_e\\ &=v_0+\frac{y_f(x)-y_b(x)}{c_t\tau_e}\\ &\quad\times\left[1+\left(-E_\parallel/c_t+E_\perp/c_t\left.\frac{dy_f}{dx}\right|_x\right)\right]. \end{aligned} \tag{136}$$

The last term is the modification of v on the back interface coming from the external field.

When Eq. (136) is taken into account, the back equation in the tip region reads (using as before space variables scaled by ϵ/c_0)

$$\begin{aligned} \frac{d^2y_b}{dx^2}&=[\cdots]_{\rm old}-B\frac{c_0}{c_t}[y_f(x)-y_b(x)]\\ &\quad\times\left[-E_\parallel/c_t+E_\perp/c_t\left.\frac{dy_f}{dx}\right|_x\right]\left[1+\left(\frac{dy_b}{dx}\right)^2\right]^{3/2}, \end{aligned} \tag{137}$$

where $[\cdots]_{\rm old}$ denotes the terms on the right-hand side of Eq. (22). When the front and back equations are linearized around the critical finger as $y_f(x)=Y_f(x)+\delta y_f(x), y_b(x)=Y_b(x)+\delta y_b(x)$ one obtains as before $\delta y_f(x)=\eta_1\delta c_t/c_0$ [Eqs. (25) and (32)] and a modified equation for $\delta y_b(x)$,

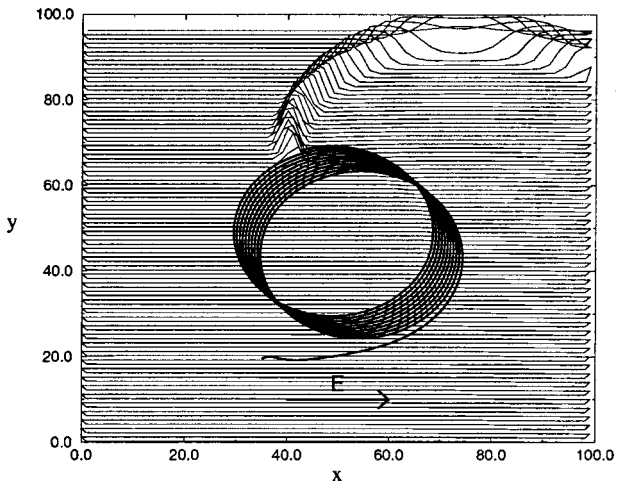

FIG. 14. Simulation of the FN model of Fig. 1 ($\epsilon=0.185,\delta=-1.41$) with an external field added as in Eq. (127) with $E=1.0\times10^{-3}$. The wave tip trajectory is shown (bold line) as well as surface plots of u showing the spiral position at the end of the simulation. The spiral is found to drift at about 135° with the field in good agreement with the present asymptotic prediction of 132.5°.

$$\mathcal{L}_b(\delta y_b)=[\cdots]_{\rm old}-B_c[Y_f(x)-Y_b(x)]\times\left[-E_\parallel/c_0+E_\perp/c_0\left.\frac{dY_f}{dx}\right|_x\right]\left[1+\left(\frac{dY_b}{dx}\right)^2\right]^{3/2}. \tag{138}$$

Integrating both sides of Eq. (138), one obtains the solvability condition which replaces Eq. (35),

$$\frac{\delta c_t}{c_0}[I_1+B_c(-I_2+I_3)]-\delta B I_3=B_c(-E_\parallel/c_0 I_3+E_\perp/c_0 I_\perp), \tag{139}$$

where the constants I_1,I_2,I_3 have previously been defined [Eq. (36)] and the new constant $I_\perp$ is given by the integral

$$I_\perp=\int_0^{+\infty}dx\,\xi(x)[Y_f(x)-Y_b(x)]\frac{dY_f}{dx}\left[1+\left(\frac{dY_b}{dx}\right)^2\right]^{3/2}\simeq 8.431. \tag{140}$$

Equation (139) shows that Eq. (129) holds with the following expressions for $\gamma_\parallel$ and $\gamma_\perp$:

$$\gamma_\parallel=-\frac{B_c}{K}\simeq-0.850,\qquad \gamma_\perp=\frac{B_c I_\perp}{K I_3}\simeq 0.929. \tag{141}$$

Changes of spiral core radius are the dominant effect in the large core limit and lead to a drift opposite to the field ($\gamma_\parallel<0$) as qualitatively argued in [25]. We quantitatively find here that a counterclockwise rotating spiral drifts at an angle of about 132.5° with the field direction in good agreement with previous simulations [25] as well as our own, as shown in Fig. 14 (the sign of $\gamma_\perp$ and of the drift angle would be opposite for a clockwise rotating spiral).

Finally, we note that the curvature-induced motion of a weakly curved three-dimensional (3D) scroll wave [46,37] filament is directly related to spiral drift in an electric field. For a 3D filament $(x_0(s),y_0(s),z_0(s))$, we can choose a coordinate system with its third axis aligned with the filament tangent at s. Locally, the activator field can be written $u(x-x_0(s),y-y_0(s);t)$ with $u(x,y;t)$ a two-dimensional spiral wave. The two-dimensional Laplacian in Eq. (3) acting on such a solution gives $\nabla^2_{2D}u-(x''\partial_x+y''\partial_y)u=\nabla^2_{2D}u-\kappa\mathbf{N}\cdot\boldsymbol{\nabla}u$ where κ is the filament curvature and N the filament normal with κN directed toward the filament center of curvature. Therefore, $\epsilon\kappa N$ acts as an external field E in the normal (x,y) plane. Since $\gamma_\parallel<0$ and a spiral drifts opposite to the field direction, one concludes that a scroll ring grows and that curvature is destabilizing in the large core limit (negative line tension). Moreover, a scroll ring propagates normally to the plane of the ring at a velocity proportional to its expansion velocity since $\gamma_\perp\neq0$. The other laws governing filament motion can similarly be deduced by reducing the 3D dynamics to an effective 2D process. We defer, however, a detailed study of 3D dynamics in the large core limit to a future publication.

VIII. MULTIARMED SPIRALS

In this section we extend our analysis to the situation where several thin excited regions or ''spiral arms'' rotate around a common core. Our main finding is that such multiarmed spiral waves are always linearly unstable in the large core limit. We confirm this finding by numerical simulation of the FitzHugh-Nagumo model for two-arm and three-arm spirals. A different conclusion has been reached in Ref. [26] where multiarmed spiral waves were found by numerical simulation of the FN model, with a well-prepared initial condition, to be stable over windows of parameters in the large core limit. We shall comment at the end of this section on the possible origin of this disagreement.

Let us denote by $q_j(\theta)$ the coordinate of the tip of the jth spiral arm. We make the arbitrary choice that rotation is counterclockwise and take the index $j\in[0,N-1]$ to increase clockwise. The equation for the phases, $\psi_j=\theta_j-\omega_1 t$, is given by

$$d\psi_j/dt=-(\epsilon/c_0R_0)\omega_1 q_j\quad(j=0,\ldots,N-1). \tag{142}$$

For simplicity, we consider an initial condition where the angular positions of the N spiral arms are uniformly distributed. To lowest order in $\epsilon/(c_0R_0)$, one can assume that the spiral arms rotate at constant angular velocity and that the phase difference between two successive arms remains constant: $\psi_j-\psi_{j-1}=2\pi/N$. The equation that governs the motion of a given arm, say arm j, is essentially the same as the one governing the motion of a one-arm spiral, except that this arm interacts with the exponential recovery tail of the controller field v of arm $j-1$, instead of its own recovery tail. Consequently, the equation of motion for arm j is simply obtained by replacing the interaction term $mF(q(\theta)-q(\theta-2\pi))$ on the right-hand side of Eq. (85) by $m_NF(q_j(\theta)-q_{j-1}(\theta-2\pi/N))$, with m_N defined in terms of the reduced

period $2\pi R_0/N$. For a spiral with N arms, the wave tips are governed by the N coupled equations

$$\frac{d^2q_j}{d\theta^2}+q_j=m_N F(q_j(\theta)-q_{j-1}(\theta-2\pi/N))$$

$$(j=0,\ldots,N-1), \tag{143}$$

where

$$m_N=\frac{3B_c(bK)^{3/2}}{2(B_c-B)^{5/2}}\exp\left[-\frac{2\pi\epsilon}{c_0^2N\tau_R}\left(\frac{bK}{B_c-B}\right)^{3/2}\right] \tag{144}$$

and F is the same function as for a one-arm spiral.

A. Linear stability

Let us first analyze the linear stability of an N-arm spiral. Linearizing Eqs. (143), we obtain

$$\frac{d^2q_j}{d\theta^2}+q_j=\alpha[q_j(\theta)-q_{j-1}(\theta-2\pi/N)]$$

$$(j=0,\ldots,N-1), \tag{145}$$

where we have defined $\alpha\equiv m_N F'(0)$. The symmetry of the above system of linear equations implies that its solutions must be of the discrete Floquet-Bloch form

$$q_j=\hat{q}\exp(ik_nj+\Omega_n\theta), \tag{146}$$

where k_n is the discrete Bloch wave vector that takes on the values

$$k_n=\frac{2\pi n}{N}\quad(n=0,\ldots,N-1). \tag{147}$$

Substituting the above form into Eq. (145), we obtain the eigenvalue equation

$$\Omega_n^2+1=\alpha\left[1-\exp\left(-\frac{2\pi}{N}(\Omega_n+in)\right)\right]\quad(n=0,\ldots,N-1) \tag{148}$$

that determines the allowed values of Ω_n for each mode n and hence its stability. The two global translational modes, which are exact solutions of Eq. (148) for arbitrary α, correspond to $\Omega_1=-i$ and $\Omega_{N-1}=i$. We restrict ourselves to considering the $2N-2$ other modes which correspond to the coupled translations of the individual spiral arms. The eigenvalues corresponding to these modes can be calculated perturbatively by expanding Ω_n in a power series in α about $\pm i$. For brevity of notation, let us denote by Ω_n^+ the $N-1$ eigenvalues obtained by expanding about $\Omega_1=+i$ for $n=0,2,\ldots,N-1$, and by Ω_n^- the ones obtained by expanding about $\Omega_{N-1}=-i$ for $n=0,1,\ldots,N-2$. Substituting the power series expansions

$$\Omega_n=\pm i+\alpha\Omega_{n(1)}^{\pm}+\alpha^2\Omega_{n(2)}^{\pm}+\cdots \tag{149}$$

into Eq. (148) we obtain after simple algebraic steps

$$\Omega_{n(1)}^{\pm}=\pm\frac{1}{2}\sin\left(\frac{2\pi(n\pm1)}{N}\right)\mp i\sin^2\left(\frac{\pi(n\pm1)}{N}\right). \tag{150}$$

Since the leading term in the expansion (149) is purely imaginary, the stability is determined by the sign of the real part of $\Omega_{n(1)}$. Equation (150) implies that $\mathrm{Re}(\Omega_{n(1)}^-)>0$ for $n=0$ or $n>N/2+1$, and $\mathrm{Re}(\Omega_{n(1)}^+)>0$ for $n<N/2-1$, and therefore that N-arm spirals are always unstable for $N>2$. For the special case $N=2$ and $n=0$, Eq. (150) implies that $\mathrm{Re}(\Omega_{n(1)}^+)=0$, in which case the stability is determined by the sign of the real part of the next order term in the expansion, $\mathrm{Re}(\Omega_{n(2)}^{\pm})$. The calculation at order α^2 yields that $\Omega_{0(2)}^{\pm}=\pi/2\mp i/2$ and therefore that $\mathrm{Re}(\Omega_{0(2)}^{\pm})=\pi/2>0$. Thus the symmetric ($n=0$) mode is always linearly unstable for a two-arm spiral. In contrast, for the antisymmetric ($n=1$) mode, $\Omega_1=\pm i$ remains the solution for arbitrary α. We conclude that N-arm spiral waves are always linearly unstable for $N>1$ in the large core limit.

The nature of the linearly unstable tip trajectories is simple to deduce from the above results. To be concrete, let us consider two-arm and three-arm spirals that we shall study in simulations below. For $N=2$, aside from the two translational modes, there are two unstable modes corresponding to the complex conjugate pair,

$$\Omega_0^{\pm}=\pi\alpha^2/2\pm i(1-\alpha-\alpha^2/2)\quad(N=2). \tag{151}$$

Since this pair corresponds to $n=0$, the two tips will move symmetrically (with equal radial displacements) about a fixed center of rotation. Furthermore, since the imaginary part of $\Omega_0^{\pm}$ is slightly less than unity, the two tips will oscillate in and out of the unperturbed steady-state circle of rotation with a period slightly larger than the basic period T_0, and with an amplitude of oscillation that grows exponentially in time. For $N=3$, there are four modes aside from the two global translational modes: a complex conjugate pair with a negative real part, which is stable, and the unstable complex conjugate pair

$$\Omega_0^{\pm}=\sqrt{3}\alpha/4\pm i(1-3\alpha/4)\quad(N=3) \tag{152}$$

obtained by evaluating Eq. (150) for $N=3$, where the tips move with equal radial displacements. As for $N=2$, the finite imaginary part slightly smaller than unity implies that the tips will exhibit exponentially growing oscillations with a period slightly larger than T_0.

In addition, α is typically much smaller than unity in the large core limit since the spiral period is large compared to the recovery time, $\tau_R\ll T_0/N$, and the spiral arms are only weakly coupled via the controller field v. Therefore, the instability of a multiarmed spiral should generically develop on a time scale much longer than T_0, especially for $N=2$ since the real part of $\Omega_0^{\pm}$ scales as α^2, instead of as α for $N>2$.

B. Numerical simulations

In order to test the above predictions, we investigate numerically the stability of spiral waves with two and three arms in the FN model. We restrict ourselves to a range of

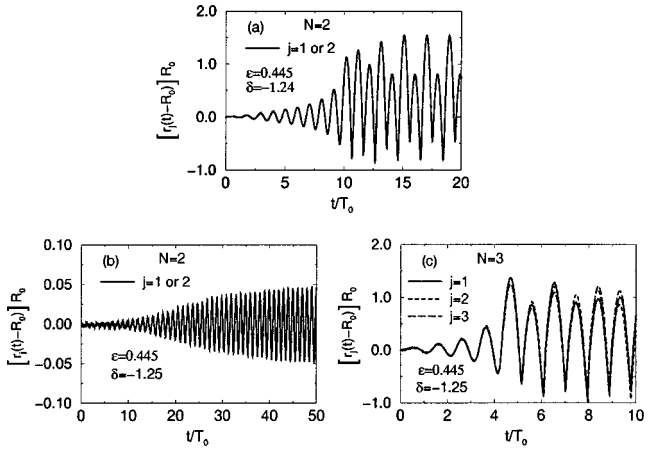

FIG. 15. Plots of the radial displacement of the wave tips vs time for two-arm [(a) and (b)] and three-arm (c) spirals. The highly nonlinear symmetric meander dynamics of three-arm spirals [Fig. 17(b)] is destabilized at large enough time leading to the elimination of one arm at boundaries. In contrast, the symmetric meander dynamics of two-arm spirals is stable on the time scale of our simulations despite the collisions illustrated in Fig. 18.

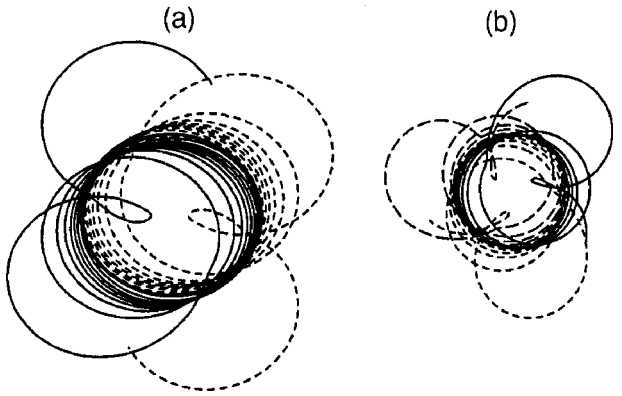

FIG. 17. Simulations of the FN model showing the wave tip trajectories during the initial development of the instability of multiarm spirals for (a) a two-arm spiral with $\epsilon=0.445$ and $\delta=-1.24$, and (b) a three-arm spiral with $\epsilon=0.445$ and $\delta=-1.25$. Each line type (solid, dashed, or long-dashed) corresponds to a different wave tip trajectory.

parameters where a one-arm spiral is linearly stable and rotates rigidly. We construct an initial condition for an N-arm spiral, denoted by (u_N, v_N), by simply rotating $N-1$ times by $2\pi/N$ a one-arm spiral wave, which yields the expressions

$$u_N(r,\theta)=\sum_{j=0}^{N-1} u(r,\theta-2\pi j/N)-(N-1)u_0, \quad (153)$$

$$v_N(r,\theta)=\sum_{j=0}^{N-1} v(r,\theta-2\pi j/N)-(N-1)v_0, \quad (154)$$

where (u_0, v_0) are as before the resting values of u and v. Since the simulations are performed in Cartesian coordinates, and the edges have a negligible effect, each rotation of $2\pi/N$ is simply carried out by running the simulation of a one arm spiral for a time equal to T_0/N. The initial condition defined by Eqs. (153) and (154) deviates from the true steady-state solution of an N-arm spiral by an amount proportional to $v-v_0$ on the wave fronts, which is exponentially small in the large core limit. Therefore, this initial condition can be considered as a slightly perturbed N-arm spiral solution and is ideal for the present purposes.

Results of the simulations are shown in Fig. 15 where we plot the normalized radial displacement of the wave tips, $[r_j(t)-R_0]/R_0$, which corresponds to $\epsilon q_j/c_0$ in our analysis. We calculated the position of the N wave tips by looking for the points of zero normal velocity along the spiral boundary defined by $u=0$. This is equivalent to looking for the N intersections of the curves $u=0$ and $\partial_t u=0$. We measured $r_j(t)$ from the instantaneous center defined by $\bar{x}(t)=\Sigma_{j=1}^{N} x_j(t)/N$ and $\bar{y}(t)=\Sigma_{j=1}^{N} y_j(t)/N$. All the main qualitative features predicted by our analysis are observed in the simulations. (We have not attempted a detailed quantitative comparison because our predictions are strictly valid outside the range of our simulations.) First, during the initial instability, the center of rotation $(\bar{x}(t),\bar{y}(t))$ remains fixed in time and the radial displacements are equal for all tips. This implies that the symmetric $n=0$ is the most unstable one. Secondly, the radial displacements exhibit exponentially amplified oscillations, with the amplification rate depending sensitively on the steady-state period T_0 and the number of arms, which both determine the parameter, $\alpha=F'(0)m_N$, entering in the predicted amplification rates [i.e., the real parts of $\Omega_0^{\pm}$ in Eqs. (151) and 152)]. In particular, Fig. 15 shows that the amplification is much slower in (b) than (a), which agrees with the fact that T_0 is about 1.46 times larger in (b) than (a). In addition, for the same parameters, the three-arm spiral in (c) is destabilized much faster than the two-arm spiral in (b), in agreement with the fact that m_N defined by Eq. (144) is larger for $N=3$ than $N=2$. Lastly,

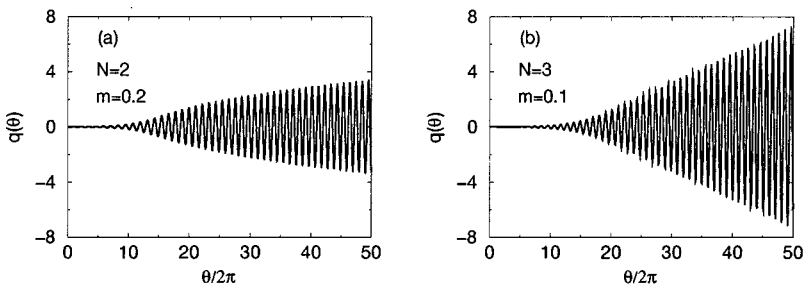

FIG. 16. Plot of $q(\theta)$ vs $\theta/2\pi$ obtained by numerical integration of the wave tip equation with F defined by Eq. (121) and $a=0.2$; (a) two-arm spiral for $m=0.2$, and (b) three-arm spiral for $m=0.1$.

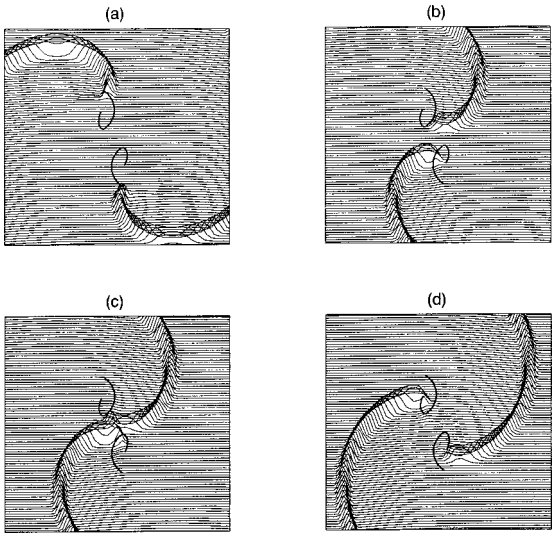

FIG. 18. Sequence of surface plots of u and superimposed wave tip trajectories (thick solid lines) illustrating the highly nonlinear collision of wave fronts occurring during a symmetric meander pattern of a two-arm spiral. Simulation parameters are $\delta=-1.24$ and $\epsilon=0.445$. Frames (b), (c), and (d) are at $t/\epsilon=20$, 25, and 40, respectively, with t measured from frame (a). Note that an exchange of wave tips and spiral arms occurs during the collision in (c), such that the wave tip of the downward moving arm in (b) is at the end of the upward moving arm in (d) and vice versa. This exchange produces the sharp pivot turns around the small inward meander petals.

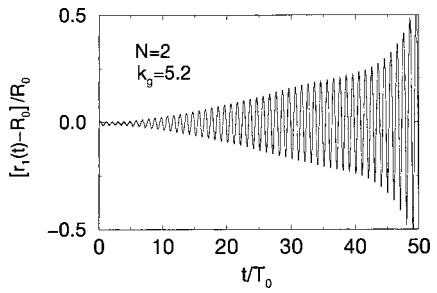

FIG. 19. Plot of the radial displacement of one of the spiral tips vs time showing the instability of a two-arm spiral wave in the FN kinetics studied in Ref. [26]. The kinetics is defined by the equations $\partial_t g=D\nabla g-k_r g(g-a)(g-1)-k_r g$ and $\partial_t r=(g-r)/\tau$. We used $k_g=5.2$ and the other parameters as defined in Ref. [26]: $D=1$, $k_r=1.5$, $a=0.05$, and $\tau=5$.

the period of the radial oscillation is slightly larger than T_0 as predicted by our analysis. This can be seen, for example, in Fig. 15(b) where the radial displacement of the tips exhibits 48 peaks over a time lapse of $50T_0$.

One interesting question is whether the instability of the symmetric mode saturates in a nonlinear regime. To explore this question, we have integrated Eq. (143) numerically for the symmetric mode by letting $q_1(t)=q_2(t)=\cdots q_N(t)\equiv q(t)$, in which case Eq. (143) reduces to a single equation for $q(t)$. We investigated different values of N and m for the function F defined by Eq. (121) with $a=0.2$. The results are shown in Fig. 16 for $N=2$ and $N=3$, the plots for higher N being qualitatively identical to the plot for $N=3$. These plots show that the bifurcation is subcritical. For all $N\geqslant 2$, the amplitude of oscillation increases linearly in time in the nonlinear regime. This comes about because in the forced harmonic oscillator equation for q the amplitude of the resonant forcing term F saturates when q becomes of order one. For small m_N, averaging the forcing term over one period of the harmonic motion gives the mean energy increase of the oscillator and accounts for the phenomenon. Interestingly, the cross over from the linear to the nonlinear regime is qualitatively different for $N=2$ and $N>2$. For $N>2$, the slope of the envelope of the oscillations increases monotonously in time until it reaches a constant value in the nonlinear regime, whereas for $N=2$, the slope of the envelope increases nonmonotonously with time. The FN simulation for $N=2$ shows qualitatively the same nonmonotonous increase of the envelope of radial oscillations with time as obtained by integrating the wave tip equation, as can be seen by comparing Fig. 15(b) and Fig. 16(a). This shows that even relatively fine details of the nonlinear instability of multiarmed spiral waves are captured by our analysis. In Fig. 15(a), the oscillations grow too rapidly to their saturated values to observe this crossover.

One important consequence of the absence of a weakly nonlinear saturation of the unstable symmetric mode is that the distance of closest approach between the wave tips (which occurs at the minimum of each oscillation) decreases with time. The resulting highly nonlinear regime is obviously not described by the wave tip equation (143), which is only valid for small radial displacements of the wave tip compared to R_0. Results of the FN simulations show the complexity of the dynamics in this regime, as illustrated by Figs. 17 and 18.

To conclude, let us contrast our results to those of Ref. [26] where the stability of multiarm spiral waves was studied in a slightly different version of FN kinetics, but in a similar regime of weak excitability. When starting from sufficiently well-prepared initial conditions, multiarmed spiral waves were found to be stable when the period T_0 was large enough to accommodate a finite number of arms around a single core. Moreover, it was observed that a spiral with N arms became unstable and decayed into a spiral with $N-1$ arms when a transition line was crossed by decreasing T_0 in the plane of T_0 and the refractory period (defined as the minimum interval between waves in response to the lowest stimulus exciting the medium), with a separate line for each N. The main difference in our predictions is that steadily rotating multiarmed spiral waves are always linearly unstable for $N\geqslant 2$ for any parameters in this plane. Note, however, that steadily rotating multiarmed spirals were not observed in [26] when starting from randomly broken arms.

We have actually checked that the instability predicted by our analysis, and observed in our FN simulations, also occurs in the FN kinetics studied in [26]. This is illustrated in Fig. 19 for a two-arm spiral and $k_g=5.2$, other parameters being chosen the same as in Ref. [26]. The main difficulty in observing this instability is that it develops extremely slowly when the spiral period is much larger than the refractory period, in which case m_N defined by Eq. (144) becomes exponentially small, and the time to observe the instability exponentially large, as a function of the ratio of the two periods. For example, for the parameter of Fig. 19, the destabilization of the two-arm spiral already occurs over a

time scale of about ten rotations. For the value $k_g=5$ reported in Fig. 3 of [26], T_0 is about twice larger than for $k_g=5.2$. Hence, the instability cannot be seen on a time scale of a few rotations.

IX. TOWARD SMALLER CORE RADII: A DISCUSSION

We have seen in Sec. VI that the large core equation of motion (85) lead to a meander onset frequency ω_2 which is equal to half the basic spiral frequency, quite independently of the detailed form of the function F. It is interesting to identify the main subdominant effects which leads ω_2/ω_1 to depart from 1/2 for smaller core radius (as shown in Fig. 9). The following two assertions underlie the large core result.

(i) The tangential velocity and spiral tip rotation rate only depend on the instantaneous characteristics of the medium in which the spiral tip propagates (i.e., the relaxation of the tip velocity and rotation rate can be taken to be instantaneous).

(ii) The angular tip position is slaved to time ($\theta=\omega_1 t$), i.e., the time interval between two successive passages of the spiral tip by the same angular position θ can be taken to be $2\pi/\omega_1$ and one can neglect the dependence of this time interval on the spiral path.

A systematic discussion of corrections to the large core limit is beyond the scope of this article. We content ourselves here in showing that corrections to (i) and (ii) both affect the value of ω_2/ω_1 at onset. As discussed below, taking into account the noninstantaneous relaxation [i.e., corrections to (i)] formally appears to give the dominant correction to the large core limit results. However, corrections to (ii), although subdominant, seem the most important for the parameter range of Fig. 9 and account semiquantitatively for the numerical results.

We begin by discussing (i). The motion of the spiral tip is determined from the two relations (63), (64). The tangential tip velocity is determined by the dynamics of the close tip region $\sim\epsilon/R_0$, which is fast and independent of the spiral core size. The determination of the radius of curvature of the spiral tip trajectory involves, however, the dynamics of a whole intermediate region $\sim(R_0R_{\rm tip}^2)^{1/3}$ and, as discussed in Appendix B, this happens on a time scale t_d with $\omega_1 t_d/\sim(R_{\rm tip}/R_0)^{1/3}$. So one expects that this instantaneous radius of curvature, which we denote here by $\tilde{R}_i$ to distinguish it from the steady-state value R_i, adapts on a time scale t_d to changes in medium conditions. Short of solving Eq. (B2), a crude model of this effect is obtained by replacing the instantaneous Eq. (64) by

$$t_d\frac{d\tilde{R}_i}{dt}+\tilde{R}_i=R_i[c_t(\{v\})]. \tag{155}$$

This gives instead of Eq. (70) the couple of equations

$$\frac{d^2q}{d\theta^2}+q=\delta\tilde{R}_i c_0/\epsilon, \tag{156}$$

$$\omega_1 t_d\frac{d(\delta\tilde{R}_i)}{d\theta}+\delta\tilde{R}_i=\delta R_i, \tag{157}$$

where δR_i is given by Eqs. (71), (84), as previously. At the linear level, Eq. (157) simply becomes

$$\omega_1 t_d\frac{d(\delta\tilde{R}_i)}{d\theta}+\delta\tilde{R}_i=\alpha\frac{\epsilon}{c_0}[q(\theta)-q(\theta-2\pi)]. \tag{158}$$

Searching for the eigenmodes of Eqs. (156), (158) under the form $q=A\exp(\sigma\theta)$ gives the modified eigenvalue equation

$$(\sigma^2+1)(1+\sigma\omega_1\tau_d)=\alpha[1-\exp(-2\pi\sigma)]. \tag{159}$$

The meander threshold is determined by requiring that Eq. (159) has purely imaginary roots $\sigma=i\Omega$ besides the two translation modes $\sigma=\pm i$. Perturbation around the large core ($t_d=0$) result gives the modification to the meander frequency at onset,

$$\Omega=\frac{1}{2}-\frac{\omega_1\tau_d}{2\pi}. \tag{160}$$

So relaxation effects lower the frequency ratio ω_2/ω_1 below 1/2 and cannot account for the numerical observations reported in Fig. 9.

In contrast, we show that improving on (ii) leads to corrections in agreement with the numerical data. We parametrize the spiral tip position as in Sec. V A as $z=(R_0+\epsilon q/c_0)\exp\{i[\omega_1 t+\psi(t)]\}$. The angular tip position is

$$\theta=\omega_1 t+\psi(t). \tag{161}$$

Beyond leading order, $\psi(t)$ is not negligible in Eq. (161) and the spiral period of rotation T depends on the spiral tip path. Equation (67) gives $\dot{\psi}=-\omega_1 q/R_0$ to dominant order [near the meander onset the other term in Eq. (67) is of higher order, $\delta c_q/c_0\sim(\epsilon/c_0R_0)^{5/3}$ using Eqs. (70), (71) and it can be neglected]. This implies that it actually takes a time $T=T_0+\Delta T$ longer (shorter) than the period T_0 of the steady spiral to return to the same θ for outward (inward) displacements

$$\Delta T=T_0\frac{\epsilon}{c_0R_0}\int_{\theta-2\pi}^{\theta}\frac{d\phi}{2\pi}q(\phi). \tag{162}$$

This reduces (increases) the interaction with the previous tip by $\sim\Delta T/\tau_R\exp(-T_0/\tau_R)$ and causes the spiral tip to return sooner inside (outside) the core. This leads ω_2/ω_1 to move away from 1/2 toward unity. In order to explicitly show this, we compute the variation of the tip trajectory radius of rotation δR_i due to the spiral displacement taking Eq. (162) into account. Comparing Eqs. (83) and (162) gives

$$\frac{\delta R}{R_0}=\frac{3B_c}{2bK}\left(\frac{R_0c_0}{\epsilon}\right)^{2/3}\exp(-T_0/\tau_R)\times\left\{F(q(\theta)-q(\theta-2\pi))-\frac{\Delta T}{\tau_R}\frac{2K+JB_c}{B_c}\right\}. \tag{163}$$

A modified version of Eq. (85) is obtained by substituting Eq. (163) in Eq. (69),

$$\ddot{q}+\omega_1^2 q=m\omega_1^2\left\{F[q(\theta)-q(\theta-2\pi)]-\frac{\Delta T}{\tau_R}\frac{2K+JB_c}{B_c}\right\}, \tag{164}$$

where the constant m is given by Eq. (87) and ΔT depends on the tip trajectory [Eq. (162)]. The linear version of Eq. (164) is (where we can replace time by angular position)

$$\frac{d^2q}{d\theta^2}+q=\alpha[q(\theta)-q(\theta-2\pi)]-\beta\int_{\theta-2\pi}^{\theta}\frac{d\phi}{2\pi}q(\phi), \tag{165}$$

where $\alpha=mF'(0)$ as before and $\beta=m(T_0/\tau_R)(\epsilon/c_0R_0)(2K+JB_c)/B_c$. The eigenmodes of Eq. (165) are of the form $q(\theta)=A\exp(\sigma\theta)$ where σ is a solution of

$$\sigma^2+1=\left(\alpha-\frac{\beta}{2\pi\sigma}\right)[1-\exp(-2\pi\sigma)]. \tag{166}$$

The meander onset corresponds to the critical value α_c where Eq. (166) has purely imaginary roots $\sigma=i\Omega$ (besides the two translation modes $\sigma=\pm i$). For small β, first-order perturbation around the $\beta=0$ values gives

$$\alpha_c=\frac{3}{8}-\frac{4\beta}{3\pi^2}, \tag{167}$$

$$\Omega=\frac{1}{2}+\frac{8\beta}{3\pi^2}. \tag{168}$$

This shows that the correction term in Eq. (164) lowers the threshold for the meander instability (i.e., plays a destabilizing role). More importantly, it increases the frequency ratio $\Omega=\omega_2/\omega_1$ at meander onset, as announced.

The frequency shift predicted by Eq. (168) can be compared to the numerical results of Fig. 9. Using the lowest-order threshold estimate $mF'(0)=3/8$, one obtains $\Omega-1/2\simeq\epsilon/[c_0c_t\tau_RF'(0)]$. With the estimate $F'(0)\sim-0.58\ln(\Delta)$, the frequency shift is found to be of the same order of magnitude as the one measured. This semiquantitative agreement leads us to think that, for the parameters of Fig. 9, the correction (168) is the main effect and that the correction (160) is still numerically smaller than Eq. (168). Of course, for spirals of sufficiently large core this should cease to be true, the correction (160) should become dominant, and ω_2/ω_1 is expected to drop below 1/2 before ultimately reaching its asymptotic value. Unfortunately, a numerical check of this nonmonotonic behavior would require simulating spirals of very large core radius. This appears a difficult task with present-day computers.

X. CONCLUSION

We have developed an analytical approach to spiral waves close to the line ∂R where the spiral rotates around a large core and in the free-boundary limit where the medium exhibits an abrupt response to a stimulus ($\epsilon\ll1$). The main ingredient of our analysis has been to note that in this limit the entire wave tip can be treated as an essentially rigid body, the slow motion of which is controlled by the local spatial gradient of excitability in the medium in a way that can be precisely deduced from the starting reaction-diffusion equations. This has provided a simple understanding of the spiral tip motion and a precise reduction of its dynamics to that of a single point. This has allowed us to describe the Hopf bifurcation nature of the meander instability and to derive simply, but with precise asymptotic estimates, spiral drift due to spatial or temporal variation of excitability, or due to an imposed external field. This last computation determines in particular the drift angle of the spiral with the external field and also the parameters governing the motion of an average scroll wave filament (curvature has been found to be destabilizing in the large core regime). In addition, our analysis has allowed us to elucidate a generic instability of multiarmed spiral waves that was previously missed in numerical simulations in the large core limit because it develops very slowly.

The present analysis can be compared with several previous analytical approaches which have provided insights into spiral wave dynamics. As already noted, a phenomenological kinematical model of spiral wave dynamics [18] has been proposed several years ago and has succeeded in capturing many aspects of spiral wave motion. It differs from the present approach not only because its parameters need to be adjusted and cannot be obtained from the underlying reaction-diffusion equation but also more fundamentally because here the dynamics of the spiral tip is reduced to an ordinary differential equation (ODE) and drives the motion of the rest of the spiral arm whereas in the kinematical model of [18] the tip motion follows from that of the whole curve. Moreover, the tip motion is described here in a different way, by the tip rotation rate and not by a growing or retracting velocity as in [18]. Another notable approach is based on normal forms [16]. As in our case, the tip motion is described by ODE. The normal form approach postulates the existence of a Hopf bifurcation and it describes its coupling to the spiral translation modes and the resulting tip motion based on general symmetry arguments, close to the resonant case where the meander frequency ω_2 is equal to the basic spiral rotation frequency ω_1. The present approach is restricted to a particular limit but makes more specific predictions. Besides providing determined parameters in the reduced equation which gives, for instance, the drift angle with an external field, it has the advantage, in our view, of providing an understanding of the physical mechanisms responsible for the very existence of spiral waves and of their dynamics, be it meander or drift due to external action.

Extensions of the present work can be considered in several directions.

(1) It would be interesting to extend the analysis to slightly more excitable media to capture hypermeandering or at least the change from inward to outward petals (i.e., the line $\omega_1=\omega_2$). This would require going beyond our adiabatic approximation and considering the dynamics of the intermediate region.

(2) The large core nature of the spiral rotation (i.e., the proximity of the line ∂R) is an essential element of our approach but several of our arguments do not really require sharp front and back interfaces (i.e., $\epsilon\ll1$). This is certainly true for the $-3/2$ divergence of the spiral radius divergence near the line ∂R which only requires that the spiral normal

velocity and curvature be related by an eikonal equation of the type of Eq. (5) on a sufficiently large scale. This is also the case for the validity of the adiabatic approximation. Thus, it appears that a computation of critical fingers and of the allied solvability conditions at finite ϵ would provide an extension of our reduced description to the neighborhood of the full line ∂R. This would not accurately describe meander (since ∂R and ∂M are close only for $\epsilon \ll 1$) but would allow a simple quantitative description of spiral drift and other phenomena along this line.

(3) Finally, it appears possible to extend some of our calculations to scroll waves in 3D as succinctly described for filament motion in Sec. VII B. Hopefully, this will not only provide definite coefficients in the average filament equations of motion, but it will also provide a better understanding of the dynamics and instabilities of 3D scroll filaments [47,37,48,49].

ACKNOWLEDGMENTS

We are grateful to B. Pier for performing some computations at an early stage of this work. The work of A.K. is supported by the American Heart Association.

APPENDIX A: THE TIP BOUNDARY LAYER

It has been noted in Sec. IV A that the solutions of the free-boundary problem (5), (8) are continuous as well as their first two derivatives but have a discontinuous third derivative at their tip. We show in this appendix that this weak nonanalyticity can be taken care of by introducing a boundary layer of size $\epsilon/\sqrt{c_0} \sim \epsilon^{5/6}$ near the wave tip (i.e., smaller than the tip radius of curvature of size $\epsilon/c_0 \sim \epsilon^{2/3}$ and larger than the interface width $\sim \epsilon$).

We restrict ourselves to analyzing the case of a critical finger. We take the interface width ϵ as length unit. We first consider the sharp interface case. We find it convenient to parametrize the interface as $x=h(y)$ instead of $y=y_{f/b}(x)$ as in the main part of this paper. In the vicinity of the wave tip ($h'(y) \ll 1$), Eq. (5) reduces to

$$c_0 h'(y) = c(v) - h''(y). \tag{A1}$$

The nonanalyticity of the interface is a direct consequence of the nonanalyticity of $c(v)$,

$$c(v) = \begin{cases} c_0 = -\alpha(v_0 - v_s), & y>0 \\ c_0 - 2y\dfrac{\alpha\epsilon}{c_0\tau_e} + \cdots, & y<0. \end{cases} \tag{A2}$$

Equations (A1) and (A2) give

$$h(y) = \begin{cases} \dfrac{1}{c_0}\left(\dfrac{1}{2}(yc_0)^2 - \dfrac{1}{6}(yc_0)^3 + \cdots\right), & y>0 \\ \dfrac{1}{c_0}\left(\dfrac{1}{2}(yc_0)^2 - \dfrac{1}{6}(1-2B_c)(yc_0)^3 + \cdots\right), & y<0. \end{cases} \tag{A3}$$

When one takes into account the finite width of the interface $c(v)$ becomes a rapidly but smoothly varying function in the wave tip neighborhood. For a shape moving at c_0 along the y direction the two reaction-diffusion equations (3), (4) become

$$-c_0 \partial_y u = \nabla^2 u + f(u,v), \tag{A4}$$

$$-c_0 \partial_y v = \epsilon g(u,v). \tag{A5}$$

For notational simplicity, we consider functions f and g of the form $f(u,v)=F(u)-v, g(u,v)=u-\eta$ with the stall concentration $v_s=0$ and the corresponding rest state at $u=0, v=0$. We choose $F(u)=-Au(u-1)(u-2)$ for illustrative purposes which gives $\Delta = 2A\eta$. To study the tip neighborhood, it is convenient to use instead of x the displaced coordinate $z=x-h(y)$ where $x=h(y)$ is a line in the interface transition region (for definiteness, one can take an iso-u line, for instance, the line $u=1$ with the above choice of F). Equation (A4) then reads

$$-c_0[\partial_y - h'(y)\partial_z]u = \partial_z^2 u + [\partial_y - h'(y)\partial_z]^2 u + F(u) - v. \tag{A6}$$

The controller field v is assumed to remain close to the stall concentration and in the tip neighborhood h' is small. Thus, at dominant order, Eq. (A6) reduces to

$$\partial_z^2 u + F(u) = 0, \tag{A7}$$

which has a standing front solution $u^{(0)}(z)$ which goes from $u^{(0)}=0$ at $z=-\infty$ to $u^{(0)}=u_\infty$ at $z=+\infty$ [$u^{(0)}(z) = 1 + \tanh(z\sqrt{A/2})$ for the above choice of F]. At next order, one obtains

$$\partial_z^2 u^{(1)} + F'(u^{(0)})u^{(1)} = [c_0 h'(y) + h''(y)]\partial_z u^{(0)} - h'^2(y)\partial_z^2 u^{(0)} + v. \tag{A8}$$

Integrating both members of Eq. (A8) with the zero mode $\partial_z u^{(0)}$ gives the solvability condition,

$$c_0 h'(y) = -h''(y) + c(y), \tag{A9}$$

with

$$c(y) = -\frac{\int dz\, v \partial_z u^{(0)}}{\int dz (\partial_z u^{(0)})^2}. \tag{A10}$$

When v has negligible variations in the interface width, Eq. (A10) gives back the sharp interface result with $c(v) = -\alpha v$ and

$$\alpha = \frac{u_\infty}{\int dz [\partial_z u^{(0)}]^2}. \tag{A11}$$

On the contrary, in the tip region, v varies in the interface transition region and the integral term in Eq. (A10) needs to be more carefully evaluated. To lowest order, the field v on the interface is obtained by integrating Eq. (A5),

$$v(z,y)=v_0+\frac{\epsilon}{c_0}\int_y^{+\infty}dy_1 u_0[z+h(y)-h(y_1)]. \tag{A12}$$

When Eq. (A12) is substituted in Eq. (A10), one obtains a smooth function $c(y)$,

$$c(y)=-\alpha v_0-\frac{\epsilon\alpha u_\infty}{c_0}\int_y^{+\infty}dy_1 T(h(y)-h(y_1)), \tag{A13}$$

with

$$T(w)=\int_{-\infty}^{+\infty}dz\frac{\partial_z u_0 u_0(z+w)}{u_\infty^2}. \tag{A14}$$

Equation (A14) gives a smoothly varying function (for instance with the above choice of F, $T(w)=\frac{1}{2}[\exp(w\sqrt{A/2})/\sinh(w\sqrt{A/2})-w\sqrt{A/2}/\sinh^2(w\sqrt{A/2})]$) instead of the Heaviside function of the sharp interface limit. To make further progress, we assume (and check afterwards) that $h(y)=c_0y^2/2+\eta(y)$ with η a small correction in a neighborhood of the spiral tip that can be neglected in evaluating the integral term in Eq. (A13),

$$\int_y^{+\infty}dy_1 T(h(y)-h(y_1))\simeq\int_y^{+\infty}dy_1 T(c_0y^2/2-c_0y_1^2/2)$$
$$\equiv\frac{1}{\sqrt{c_0}}S(y\sqrt{c_0}). \tag{A15}$$

Equation (A9) then gives for the tip profile correction

$$c_0^2y+c_0\eta'(y)=-\frac{\epsilon\alpha u_\infty}{c_0^{3/2}}S(y\sqrt{c_0})-\eta''(y). \tag{A16}$$

Comparing the different terms, one obtains that a consistent scaling is $y\sim 1/\sqrt{c_0}$ and $\eta\sim\sqrt{c_0}$ which give the size of the boundary layer (note that, here, our unit of length is the interface width ϵ) and the magnitude of the shape correction in the boundary layer. This legitimates the neglect of η in Eq. (A15). In the scaled variables, $y=Y/\sqrt{c_0}$ and $\eta(y)=\sqrt{c_0}H(y\sqrt{c_0})$, the equation for the tip profile correction is

$$\frac{d^2H}{dY^2}+B_cS(Y)+Y=0, \tag{A17}$$

where the function $S(Y)$ is defined by Eqs. (A15) and (A14) [the second term on the left-hand side of Eq. (A16) is of higher order]. The behaviors of S at infinity, $S(Y)\to 0$ at $Y=+\infty$ and $S(Y)\to -2Y$ at $Y=-\infty$, give the corresponding asymptotic behaviors of H, $H(Y)\to -Y^3/6$ at $Y=+\infty$ and $H(Y)\to -Y^3(1-2B_c)/6$ at $Y=-\infty$. These precisely match the different small-y behaviors [Eq. (A3)] of the sharp interface description. It shows that $H(Y)$ interpolates smoothly between these different behaviors.

APPENDIX B: DYNAMICS OF THE INTERMEDIATE REGION

The analysis of spiral dynamics that we have developed in the main part of this paper makes a crucial use of an ''adiabatic'' assumption. Namely, that for changes of medium parameter on the time scale of the spiral rotation period $T\sim R_0/c_0$, the instantaneous motion of the spiral tip can be taken to be that of a spiral tip moving in a steady medium with characteristics invariant in time and identical to those of the changing medium at the considered time. In the large core limit, the spiral is described by matching three regions: a close tip region on the scale of the tip radius $R_{\rm tip}=\epsilon/c_0$ which determines the spiral tip tangential velocity; an intermediate region of size $(R_0R_{tip}^2)^{1/3}$ which determines the instantaneous radius of curvature of the tip trajectory, and finally, an outer scale the dynamics of which is driven by the previous two regions. The close tip region relaxes on a time scale which is independent of the spiral radius and which therefore clearly becomes short compared to the spiral period T for a spiral of sufficiently large radius. In this appendix, we show that the intermediate region relaxes on a time scale $T(R_{\rm tip}/R_0)^{1/3}$ which is also much shorter than the rotation period T in the large radius limit. This justifies our adiabatic assumption.

We first write the dynamic equivalent of the static BCF equation (40), that is, the motion of a curve governed by Eq. (5) using polar coordinates

$$r\frac{\partial\theta_f}{\partial t}=c_0\left[1+\left(r\frac{d\theta_f}{dr}\right)^2\right]^{1/2}+\epsilon\left(\frac{d\theta_f}{dr}+\frac{(d/dr)(rd\theta_f/dr)}{1+(rd\theta_f/dr)^2}\right). \tag{B1}$$

As for the static case, it is convenient in the intermediate region to introduce the rescaled variables y and ξ with $\theta_f=\omega_1t+y\epsilon/(c_0R_0)$ and $r=R_0+[2R_0(\epsilon/c_0)^2]^{1/3}\xi$. Expanding the square root in Eq. (B1) and keeping terms of the dominant order gives

$$\frac{R_0}{c_0}\left(\frac{\epsilon}{2c_0R_0}\right)^{1/3}\frac{\partial y}{\partial t}+\xi+a=\frac{1}{2}\frac{d^2y}{d\xi^2}+\frac{1}{4}\left(\frac{dy}{d\xi}\right)^2, \tag{B2}$$

with

$$a=2^{-1/3}\left(\frac{c_0R_0}{\epsilon}\right)^{2/3}\frac{c_t-c_0}{c_0}. \tag{B3}$$

Equation (B2) is the dynamic equivalent of the static equation (43) determining the shape of the intermediate region. It shows that the characteristic time to adapt to changes of a (e.g., of c_t) for ξ of order unity (e.g., for the intermediate region) is $R_0/c_0[\epsilon/(c_0R_0)]^{1/3}$. It is shorter by the factor $(R_{\rm tip}/R_0)^{1/3}$ than the rotation period as announced above. It is, however, worth pointing out that this is larger than the time one may have guessed, namely, the length of the intermediate region divided by the velocity c_0. The reason is that in the intermediate region the interface is almost radial. As a consequence, the advection velocity is much smaller than c_0 and advective effects become comparable to diffusionlike effects due to surface tension [i.e., the last two terms in Eq. (B2) are of the same magnitude].

APPENDIX C: SOLVABILITY INTEGRALS AND FUNCTIONS: SOME RELATIONS

In this appendix, we recapitulate the definitions and give additional information on the several functions and integrals which have been introduced in the evaluation of solvability conditions.

The linear operators considered are $\mathcal{L}_f$ and $\mathcal{L}_b$, which comes from the linearization of the front and back equations around the critical finger in the tip region,

$$\mathcal{L}_f = \frac{d^2}{dx^2} + \left\{ -2 + 3\left[1 + \left(\frac{dY_f}{dx} \right)^2 \right]^{1/2} \right\} \frac{dY_f}{dx} \frac{d}{dx}, \quad \text{(C1)}$$

$$\mathcal{L}_b = \frac{d^2}{dx^2} - a(x) \frac{d}{dx} - b(x), \quad \text{(C2)}$$

with,

$$a(x) = \left\{ 2 + 3\{1 - B_c[Y_f(x) - Y_b(x)]\} \times \left[1 + \left(\frac{dY_b}{dx} \right)^2 \right]^{1/2} \right\} \frac{dY_b}{dx},$$

$$b(x) = B_c \left[1 + \left(\frac{dY_b}{dx} \right)^2 \right]^{3/2}. \quad \text{(C3)}$$

$Y_f(x)$ and $Y_b(x)$ are the critical finger front and back interfaces which satisfy Eqs. (18) and (19) with $B = B_c = 0.5353\ldots$. The small x behaviors of these different functions are $Y_f(x) = \sqrt{2x} + x/3 + \cdots$, $Y_b(x) = -\sqrt{2x} + x(1 - 2B_c)/3 + \cdots$, $a(x) = -3/(2x) + \sqrt{2} B_c / \sqrt{x} + \cdots$, and $b(x) = B_c/(2x)^{3/2} + \cdots$.

The zero mode $\xi(x), x \geq 0$, of the adjoint of $\mathcal{L}_b$ is the solution of

$$\mathcal{L}_b^{\dagger}(\xi) = \frac{d^2\xi}{dx^2} + \frac{d}{dx}[a(x)\xi] - b(x)\xi = 0, \quad \text{(C4)}$$

which tends to 0 when $x \to +\infty$. It is here normalized by imposing the supplementary condition $\sup_{x \geq 0}[\xi(x)] = 1$. A local analysis determines the behavior of $\xi(x)$ for small x, $\xi(x) = \xi'(0)[x - B_c/\sqrt{2} x^{3/2} \ln(x) + \cdots]$. Equation (C4) has been solved numerically by a finite- difference scheme on a nonuniform grid (with a step size decreasing to zero at small x). A graph of the obtained solution is shown in Fig. 6. The computed value of the derivative of ξ at the origin is $\xi'(0) \simeq 4.441$. An exact relation between $\xi'(0)$ and a weighted integral of ξ is obtained by integrating Eq. (C4) between $x = 0$ and $x = +\infty$,

$$\xi'(0)/2 = \int_0^{+\infty} dx \xi(x) b(x) = B_c I_4. \quad \text{(C5)}$$

The verification of Eq. (C5) serves as a check of our numerical computation.

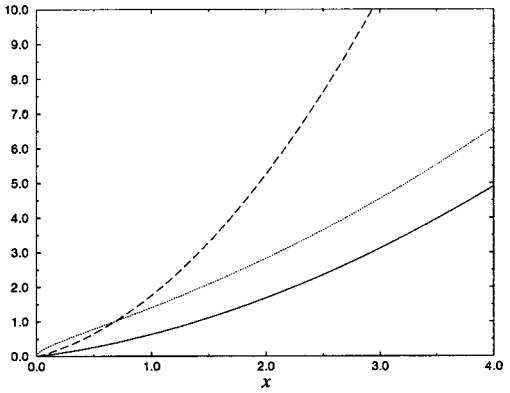

FIG. 20. Graph of the functions $\eta_1(x)$ (solid line), $\eta_2(x)$ (dotted line), and $\eta_{v,0}(x)$ (dashed line) defined in Eqs. (C6) and (C8).

To evaluate the solvability conditions, besides Y_f, Y_b, and ξ, the solutions of the following inhomogeneous equations with the linear operator $\mathcal{L}_f$ [Eq. (C1)] are needed:

$$\mathcal{L}_f(\eta_1) = 1 + \left(\frac{dY_f}{dx} \right)^2, \quad \eta_1(0) = 0, \quad \eta_1'(0) = 1/3, \quad \text{(C6)}$$

$$\mathcal{L}_f(\eta_2) = \left[1 + \left(\frac{dY_f}{dx} \right)^2 \right]^{3/2},$$

$$\eta_2(0) = 0, \ \eta_2(x) \sim \sqrt{x/2} \ \text{ for } x \ll 1, \quad \text{(C7)}$$

$$\mathcal{L}_f(\eta_{v,0}) = [Y_f(x) - Y_b(x)] \left[1 + \left(\frac{dY_f}{dx} \right)^2 \right]^{3/2},$$

$$\eta_{v,0}(0) = 0, \quad \frac{d\eta_{v,0}}{dx}(0) = 2/3, \quad \text{(C8)}$$

$$\mathcal{L}_f(\eta_e) = \frac{dY_f}{dx} \left[1 + \left(\frac{dY_f}{dx} \right)^2 \right],$$

$$\eta_e(0) = 0, \ \eta_e(x) \sim \sqrt{x/2} \ \text{ for } \ x \ll 1. \quad \text{(C9)}$$

They are plotted in Fig. 20.

For the evaluation of the different solvability conditions, it is useful to compute the following integrals:

$$I_1 = \int_0^{+\infty} dx \xi(x) \left[1 + \left(\frac{dY_b}{dx} \right)^2 \right] \simeq 2.771,$$

$$I_2 = \int_0^{+\infty} dx \xi(x) \eta_1(x) \left[1 + \left(\frac{dY_b}{dx} \right)^2 \right]^{3/2} \simeq 3.814,$$

$$I_3 = \int_0^{+\infty} dx \xi(x) [Y_f(x) - Y_b(x)] \left[1 + \left(\frac{dY_b}{dx} \right)^2 \right]^{3/2} \simeq 7.708,$$

$$I_4 = \int_0^{+\infty} dx \xi(x) \left[1 + \left(\frac{dY_b}{dx} \right)^2 \right]^{3/2} \simeq 4.1476,$$

$$I_5 = \int_0^{+\infty} dx \xi(x) \eta_2(x) \left[1 + \left(\frac{dY_b}{dx} \right)^2 \right]^{3/2} \simeq 6.306,$$

$$I_6=\int_0^{+\infty}dx\,\xi(x)\,\frac{dY_b}{dx}\left[1+\left(\frac{dY_b}{dx}\right)^2\right]\simeq -2.118,$$

$$I_{v,0}=\int_0^{+\infty}dx\,\xi(x)\,\eta_{v,0}\left[1+\left(\frac{dY_b}{dx}\right)^2\right]^{3/2}\simeq 12.553,$$

$$I_\perp=\int_0^{+\infty}dx\,\xi(x)[Y_f(x)-Y_b(x)]\frac{dY_f}{dx}\left[1+\left(\frac{dY_b}{dx}\right)^2\right]^{3/2}\simeq 8.431,$$

$$I_e=\int_0^{+\infty}dx\,\xi(x)\,\eta_e(x)\left[1+\left(\frac{dY_b}{dx}\right)^2\right]^{3/2}\simeq 4.476. \tag{C10}$$

Exact relations between some of these integrals can be obtained by using symmetry transformations of known action on the interfaces. For instance, under dilation the critical finger front and back become $Y_{f,\alpha}=Y_f(\alpha x)/\alpha$, $Y_{b,\alpha}=Y_b(\alpha x)/\alpha$ and obey scaled versions of Eqs. (18) and (19),

$$\frac{d^2Y_{f,\alpha}}{dx^2}=\alpha\left\{\left[1+\left(\frac{dY_{f,\alpha}}{dx}\right)^2\right]-\left[1+\left(\frac{dY_{f,\alpha}}{dx}\right)^2\right]^{3/2}\right\}, \tag{C11}$$

$$\frac{d^2Y_{b,\alpha}}{dx^2}=\alpha\left\{\left[1+\left(\frac{dY_{b,\alpha}}{dx}\right)^2\right]+\{1-B_c\alpha[Y_{f,\alpha}(x)-Y_{b,\alpha}(x)]\}\times\left[1+\left(\frac{dY_{b,\alpha}}{dx}\right)^2\right]^{3/2}\right\}. \tag{C12}$$

An expansion around $\alpha=1$ gives $Y_{f,\alpha}=Y_f+(\alpha-1)\,\delta Y_f+\cdots$ where $\delta Y_f(x)=xY_f'(x)-Y_f(x)$. Similarly, one has $Y_{b,\alpha}=Y_b+(\alpha-1)\,\delta Y_b+\cdots$ with $\delta Y_b(x)=xY_b'(x)-Y_b(x)$. Expanding Eqs. (C11) and (C12) in the same limit shows that δY_f and δY_b obey the following linear equations:

$$\mathcal{L}_f(\delta Y_f)=\left[1+\left(\frac{dY_f}{dx}\right)^2\right]-\left[1+\left(\frac{dY_f}{dx}\right)^2\right]^{3/2}, \tag{C13}$$

$$\mathcal{L}_b(\delta Y_b)=\left[1+\left(\frac{dY_b}{dx}\right)^2\right]+\{1-2B_c[Y_f(x)-Y_b(x)]-B_c\delta Y_f\}\left[1+\left(\frac{dY_b}{dx}\right)^2\right]^{3/2}. \tag{C14}$$

Equation (C13) shows that $\delta Y_f=\eta_1-\eta_2$ [Eqs. (C6), (C7)] since $\delta Y_f(0)=0$ (as can be checked from its explicit expression). Then, multiplying both sides of Eq. (C14) by $\xi(x)$ and integrating from $x=0$ to $+\infty$ gives the desired relation between the above integrals,

$$I_1+I_4-B_c(I_2+2I_3-I_5)=0. \tag{C15}$$

Using rotational symmetry in a similar manner, one obtains that $\eta_e(x)=x+Y_f dY_f/dx-1$ and the other relation

$$I_6+B_c(I_\perp-I_e)=0. \tag{C16}$$

In the analysis of meandering, there appear several functions of the tip displacement:

$$\mathcal{L}_f(\eta_{v,d})=[Y_f(x+d)-Y_b(x+d)]\Theta(x+d)\times\left[1+\left(\frac{dY_f}{dx}\right)^2\right]^{3/2},\quad \eta_{v,d}(0)=0, \tag{C17}$$

$$I_{3,d}=\int_0^{+\infty}dx\,\xi(x)[Y_f(x+d)-Y_b(x+d)]\Theta(x+d)\times\left[1+\left(\frac{dY_b}{dx}\right)^2\right]^{3/2},$$

$$I_{v,d}=\int_0^{+\infty}dx\,\xi(x)\,\eta_{v,d}\left[1+\left(\frac{dY_b}{dx}\right)^2\right]^{3/2}. \tag{C18}$$

For large $|d|$, these functions tend toward constant values, toward 0 when $d\to-\infty$ and $I_{3,d}\to 2I_4/B_c$ and $I_{v,d}\to 2I_5/B_c$ when $d\to+\infty$. Their behavior for small displacements ($|d|\ll 1$) is nonanalytic. From the small x behaviors of Y_f, Y_b, and ξ, one obtains, for $0<|d|\ll 1$,

$$I_{3,d}=I_3-\frac{\xi'(0)}{2}\,d\ln(|d|)+O(d), \tag{C19}$$

$$\eta_{v,d}(x)=\eta_{v,0}(x)-d\ln(|d|)+O(d). \tag{C20}$$

The expansion (C20) of $\eta_{v,d}$ for small d gives for $I_{v,d}$

$$I_{v,d}=I_{v,0}-I_4 d\ln(|d|)+O(d). \tag{C21}$$

The function F which measures the spiral self-interaction, $F(d)=(I_{3,d}+B_cI_{v,d})/I_3-J$, has therefore a singular expansion for $0<d\ll 1$,

$$F(d)\sim-\frac{2B_c}{I_3}\,d\ln(|d|)\simeq -0.576\,d\ln(|d|) \tag{C22}$$

[where we have used Eq. (C5) which shows that the singular contributions of $I_{3,d}$ and $B_cI_{v,d}$ are equal]. For $d\to-\infty$ $F(d)$ tends toward $-J\simeq-1.872$ and for $d\to+\infty$ $F(d)$ approaches $2(I_5+I_4/B_c)/I_3-J\simeq 1.774$.

The singular behavior of $F(d)$ at small d disappears when the controller field diffuses. For small diffusion $[Y_f(x+d)-Y_b(x+d)]\,\Theta(x+d)$ is simply replaced in Eqs. (C17) and (C18) by the smoother function $YS(x+d)$,

$$YS(x;\ell_D)=\int_0^{+\infty}\frac{dx'}{\sqrt{\pi}\ell_D}\exp\left(-\frac{(x-x')^2}{\ell_D^2}\right)\times[Y_f(x')-Y_b(x')]. \tag{C23}$$

For $\ell_D\ll 1$, one can check that the singular behavior of the self-interaction function is cut off at $d\sim\ell_D$ and the small distance behavior of $F(d;\ell_D)$ is

$$F(d;\ell_D)\sim-0.576\,d\ln(\ell_D). \tag{C24}$$

In the other limit $\ell_D\gg 1$, for x of order 1, $YS(x;\ell_D)\simeq 1/B_c+2x/(\sqrt{\pi}B_c\ell_D)$. The corresponding behavior of $I_{3,d;\ell_D}$ and $I_{v,d;\ell_D}$ at small d is $I_{3,d;\ell_D}=I_{3,0;\ell_D}+2I_4 d/$

$(B_c\sqrt{\pi}\ell_D)+\cdots, I_{v,d;\ell_D}=I_{v,0;\ell_D}+2I_5 d/(B_c\sqrt{\pi}\ell_D)+\cdots$. So the small distance behavior of the spiral self-interaction function is, for $\ell \gg 1$ (but still smaller than the scale of the matching region),

$$F(d;\ell_D)\sim 2\frac{I_4+B_cI_5}{B_c\sqrt{\pi}I_3}\frac{d}{\ell_D}\simeq 2.06d/\ell_D. \qquad \text{(C25)}$$

The derivative at $d=0$ of the spiral self-interaction function has been computed numerically for intermediate values of ℓ_D. It is plotted in Fig. 10.

APPENDIX D: NUMERICAL INTEGRATION OF THE WAVE TIP EQUATION

In this appendix, we describe a simple scheme to integrate numerically the equation of motion for the wave tip (85), which is convenient to rewrite as a system of first-order ordinary differential equations

$$\frac{dq}{d\theta}=p, \qquad \text{(D1)}$$

$$\frac{dp}{d\theta}=-q+mF(q(\theta)-q(\theta-2\pi)). \qquad \text{(D2)}$$

The difficulty of integrating this equation comes from the fact that the translational invariance of the underlying reaction-diffusion equations remains present in Eq. (85), and hence in Eqs. (D1) and (D2), which are invariant under the transformation

$$q(\theta)=q(\theta)+Ae^{i\theta}+\text{c.c.}, \qquad \text{(D3)}$$

where A is an arbitrary complex amplitude. It is therefore desirable to develop a numerical scheme that *discretely* preserves this symmetry in order to avoid spurious discrete effects resulting from the coupling of this translational mode to other modes. To see how to construct such a scheme, let us first consider the case where the second term on the right-hand side of Eq. (D2) is absent. In this case these equations describe simple harmonic motion with a constant energy $\sim|A|^2$. It is well known (and simple to show) that the simple Euler explicit scheme

$$q_{n+1}=q_n+hp_n, \qquad \text{(D4)}$$

$$p_{n+1}=p_n-hq_n, \qquad \text{(D5)}$$

where h is the time (angle) step, does not conserve energy, but rather pumps energy into the motion. As a result, it leads to an unbounded increase in A at long time. Therefore, this scheme violates in an obvious way the symmetry that we would like to preserve here. In contrast, the modified (Euler-Cromer) scheme

$$p_{n+1}=p_n-hq_n, \qquad \text{(D6)}$$

$$q_{n+1}=q_n+hp_{n+1} \qquad \text{(D7)}$$

exactly conserves the energy of harmonic motion. This can be seen by substituting the ansatz $p_n=p_0r^n$ and $q_n=q_0r^n$ into Eqs. (D6) and (D7). Nontrivial solutions then exist only if

$$r=1-h^2/2\pm ih\sqrt{1-h^2/4}=e^{\pm i\Delta\theta}, \qquad \text{(D8)}$$

where

$$\Delta\theta=\tan^{-1}\left(\frac{h\sqrt{1-h^2/4}}{1-h^2/2}\right). \qquad \text{(D9)}$$

Hence, $q_n^*=Ae^{in\Delta\theta}+\text{c.c.}$ is a solution of Eqs. (D6) and (D7) with constant A. Let us now extend this scheme to the case where the second term on the right-hand side of Eq. (D2) is included, by simply letting

$$p_{n+1}=p_n-hq_n+hmF(q_n-q_{n-N}), \qquad \text{(D10)}$$

$$q_{n+1}=q_n+hp_{n+1}. \qquad \text{(D11)}$$

Now the key point is that $q_n^*=Ae^{in\Delta\theta}+\text{c.c.}$ remains an exact solution of these equations only if $q_n^*-q_{n-N}^*=0$, and thus

$$\Delta\theta=2\pi/N. \qquad \text{(D12)}$$

This condition together with Eq. (D9) then uniquely fixes the step h for a given number of time steps, N, per basic period of 2π. After simple algebraic manipulations, we find that h should be equal to

$$h=2\sin(\pi/N). \qquad \text{(D13)}$$

In summary, our integration scheme is uniquely defined by Eqs. (D10) and (D11) with h given by Eqs. (D13). For an arbitrary value of N, this scheme is invariant under the transformation

$$q_n=q_n+Ae^{in\Delta\theta}+\text{c.c.}, \qquad \text{(D14)}$$

which is the direct discrete analog of Eq. (D3). A solution of a desired numerical accuracy can then be obtained by choosing N sufficiently large.

[1] A. T. Winfree, *When Time Breaks Down* (Princeton University Press, Princeton, NJ, 1987).

[2] V. S. Zykov, *Modelling of Wave Processes in Excitable Media* (Manchester University Press, Manchester, 1988).

[3] S. Jakubith, H. H. Rotermund, W. Engel, A. von Oertzen, and G. Ertl, Phys. Rev. Lett. **65**, 3013 (1990).

[4] A. T. Winfree, Science **181**, 937 (1973); W. Jahnke, W. E. Skaggs, and A. T. Winfree, J. Phys. Chem. **93**, 740 (1989).

[5] T. Plesser *et al.*, J. Phys. Chem. **94**, 7501 (1990).

[6] G. S. Skinner and H. L. Swinney, Physica D **48**, 1 (1991).

[7] A. Belmonte, Q. Ouyang, and J. M. Flesselles, J. Phys. II **7**, 1425 (1997).

[8] W. F. Loomis, *Dictyostelium Discoideum, A Developmental System* (Academic Press, New York, 1975); F. Siegert and C.

J. Weijer, Physica D **49**, 224 (1991).
[9] See, e.g., the several review articles in the focus issue of Chaos **8**, 1 (1998).
[10] R. FitzHugh, Biophys. J. **1**, 445 (1961); J. Nagumo, S. Arimoto, and S. Yoshizawa, Proc. IRE **50**, 2061 (1962).
[11] V. S. Zykov, Biofizika **31**, 862 (1986).
[12] A. T. Winfree, Chaos **1**, 303 (1991).
[13] Figure 1 was constructed from our own simulations and agrees qualitatively with the results of previous studies [11,12] regarding the existence of various boundaries between different regimes. It focuses, however, more specifically on the weakly excitable limit and thus provides a more quantitative characterization of these boundaries in this limit.
[14] E. Lugosi, Physica D **40**, 331 (1989); D. Barkley *et al.*, Phys. Rev. A **42**, 2489 (1990); Phys. Rev. Lett. **68**, 2090 (1992); I. Mitkov *et al.*, Phys. Rev. E **54**, 6065 (1996).
[15] A. Karma, Phys. Rev. Lett. **65**, 2824 (1990).
[16] D. Barkley, Phys. Rev. Lett. **72**, 164 (1994); D. Barkley and I. G. Kevrekidis, Chaos **4**, 453 (1994); V. N. Biktashev *et al.*, Int. J. Bifurcation Chaos Appl. Sci. Eng. **6**, 2433 (1996).
[17] G. Li *et al.*, Phys. Rev. Lett. **77**, 2105 (1996).
[18] See, A. S. Mikhailov, V. A. Davidov, and V. A. Zykov, Physica D **70**, 1 (1994), and references therein.
[19] K. I. Agladze, V. A. Davydov, and A. S. Mikhailov, Pis'ma Zh. Éksp. Teor. Fiz. **45**, 601 (1987) [JETP Lett. **45**, 767 (1987)]; O. Steinbock, V. Zykov, and S. C. Müller, Nature (London) **366**, 322 (1993).
[20] K. I. Agladze and P. de Kepper, J. Phys. Chem. **96**, 5239 (1992).
[21] O. Steinbock, J. Schütze, and S. C. Müller, Phys. Rev. Lett. **68**, 248 (1992).
[22] A. P. Muñuzuri *et al.*, Phys. Rev. E **50**, 4258 (1994).
[23] A. Belmonte and J. M. Flesselles, Europhys. Lett. **32**, 267 (1995).
[24] I. Mitkov, I. Aranson, and D. A. Kessler, Phys. Rev. E **52**, 5974 (1995).
[25] V. Krinsky, E. Hamm, and V. Voignier, Phys. Rev. Lett. **76**, 3854 (1996).
[26] B. Vasiev, F. Siegert, and C. Weijer, Phys. Rev. Lett. **78**, 2489 (1997).
[27] J. J. Tyson and J. P. Keener, Physica D **32**, 327 (1988).
[28] J. J. Tyson and J. P. Keener, Physica D **29**, 215 (1987).
[29] D. A. Kessler, H. Levine, and W. N. Reynolds, Physica D **70**, 115 (1994).
[30] A. Karma, Phys. Rev. Lett. **68**, 397 (1992).
[31] P. C. Fife, J. Stat. Phys. **39**, 687 (1985).
[32] P. Pelce and J. Sun, Physica D **48**, 353 (1991).
[33] A. Karma, Phys. Rev. Lett. **66**, 2274 (1991).
[34] A. Karma, in *Nonlinear Phenomena Related to Growth and Form*, edited by M. Ben Amar *et al.* (Plenum Press, New York, 1991).
[35] V. Hakim and A. Karma, Phys. Rev. Lett. **79**, 665 (1997).
[36] The numerically determined constant $\zeta \simeq 0.685$ of [18] is given in our notation by $\zeta = b'^{-3/2} = |a_1'|^{-3/2}/\sqrt{2} = 0.6876\ldots$. This value of ζ corresponds to replacing b in Eq. (13) by the constant b' given by the location a_1' of the maximum of the Airy function as explained at the end of Sec. IV C 1.
[37] V. N. Biktashev, A. V. Holden, and H. Zhang, Philos. Trans. R. Soc. London, Ser. A **347**, 611 (1994).
[38] P. Pelce and J. Sun, Physica D **63**, 273 (1992).
[39] This analysis was performed in collaboration with B. Pier, and has been described in B. Pier, DEA report (ENS Lyon), 1995.
[40] W. K. Burton, N. Cabrera, and F. C. Franck, Philos. Trans. R. Soc. London, Ser. A **243**, 299 (1951).
[41] This definition coincides with Eq. (10) since $\mathrm{Rtip} = \epsilon/c0$, $W = 2\Delta c0\,\tau e$ *with the dimensionless units of Eqs.* (3) *and* (4).
[42] *Handbook of Mathematical Functions*, edited by M. Abramowitz and I. A. Stegun (Dover, New York, 1972), p. 478.
[43] A. M. Pertsov, E. A. Ermakova, and A. V. Panfilov, Physica D **14**, 117 (1984).
[44] Note that a factor of 3 has been included in the definition of F as compared to [35]. So, the function F here defined is three times larger than in [35]. Correspondingly, the parameter m, Eq. (87) is three times smaller. Note also that here, lengths have been measured from the start on the scale of the tip radius ϵ/c_0 so that the quantities with a tilde in [35] appear here without a tilde (e.g., d here is denoted $\tilde{d}$ in [35]).
[45] D. A. Kessler and R. Kupferman, Physica D **105**, 207 (1997).
[46] J. P. Keener, Physica D **31**, 269 (1988).
[47] C. Henze, E. Lugosi, and A. T. Winfree, Can. J. Phys. **68**, 683 (1989).
[48] F. Fenton and A. Karma, Phys. Rev. Lett. **81**, 481 (1998); Chaos **8**, 20 (1998).
[49] I. Aranson and I. Mitkov, Phys. Rev. E **58**, 4556 (1998).